# Aeroelastic Response of a Contrafan Stage Using Full Annulus and Single Passage Models

Antoine Placzek, Lionel Castillon

# Aeroelastic Response of a Contrafan Stage Using Full Annulus and Single Passage Models

(Received: Feb. 25, 2014. Revised: Apr. 24, 2014. Accepted: May 5, 2014)

Antoine Placzek[1]
Lionel Castillon[2]

**Abstract**
In this paper we investigate the unsteady aeroelastic response of a contrafan stage using nonlinear time-integrated RANS equations and multichorochronic boundary conditions which are able to propagate multiple periodic perturbations with uncorrelated frequencies. The objective is to model a single passage in each blade row to reduce the computational cost and to take into account both unsteady phenomena relative to the blade passage of the neighboring blade row and to the vibration induced by the blade deformations. Numerical comparisons are performed between a full annulus reference computation of a radial slice and the present multichorochronic simulations on a single passage to check the quality of the approximation. The influence of several parameters like the number of harmonics or spinning modes is investigated. Particular attention is finally paid to the approximation of the generalized aerodynamic forces from which the aeroelastic stability can be assessed.

## 1 Introduction

Aeroelastic stability computations are usually performed on isolated turbomachinery blade rows, meaning that the effects induced by the neighboring blade rows (like wake interaction, potential effects, shock wave propagation,...) are neglected. Recent work has however pointed out the importance of modeling adjacent blade rows on stator/rotor configurations, see for example [16, 19, 24].

Multistage simulations on the full 360° annulus remain however extremely costly because of the very large number of degrees of freedom involved when the blade count is large. Numerical methods have therefore been developed since the end of the 70's to reduce the size of the computational domain. An exact reduction is possible if the blade counts of each blade row share a common multiple. This latter is however often small or even equal to one, preventing an exact reduction. Blade count reduction methods have however been developed using approximate blade counts and a rescaling of the geometry [1] or a modification of the boundary condition dealing with the pitch mismatch if the blade counts are not modified but only few blades are considered in each blade rows [8]. However these methods either modify the main flow characteristics like the mass flow because of the modification of the geometry or imply contraction/dilatation effects which may modify the frequencies.

The unsteady phenomena involved in multistage configurations are mainly due to the blade passage of the neighboring blade rows or the vibration of some structural modes which are related to the notion of traveling waves, or *spinning modes*, described in [17, 25, 29]. Based on this theory, more advanced boundary conditions have later been introduced by Erdos et al. [6] and Giles [11] for single stages using phase-lagged or "chorochronic" relations to link the flow field on azimuthal boundaries of a single passage without changing the blade count. Many improvements have then been brought to the initial formulation by He [13, 14] and Gerolymos et al. [9, 10] among others and the use of a spectral approximation (Fourier decomposition) of the flow field has become popular to avoid the storage of the flow field at many time instants. A

[1] ONERA, Aeroelasticity and Structural Dynamics Department, 29 avenue de la Division Leclerc, F-92322 Châtillon, France. antoine.placzek@onera.fr
[2] ONERA, Applied Aerodynamics Department, 8 rue des Vertugadins, F-92190 Meudon, France. lionel.castillon@onera.fr

doi:10.3293/asdj.2014.30

moving-average technique has finally been proposed [9] to compute the Fourier coefficients and recently Rahmati et al. [22] have improved the method to avoid leakage problems. Such boundary conditions have also been used to perform aeroelastic computations on *isolated* blade rows since the prescribed pattern of vibration associated to the structural eigenmodes is a traveling wave which satisfies the phase-lagged boundary conditions. These boundary conditions are consequently appropriate to deal with a single periodic phenomenon like the effect of blade passage in a rigid single stage or the vibration in an isolated vibrating blade row. He [13] and Neubauer [21] have finally extended the usual chorochronic boundary conditions to deal with several periodic phenomena (like in multistage / single vibrating stage configurations) leading to the so-called multichorochronic boundary conditions which have recently been implemented in Onera's CFD software *elsA* and validated on multistage *rigid* configurations [4]. Few attempts have been reported in the literature to model the influence of neighboring blade rows on the aeroelastic stability using a single passage model and multichorochronic boundary conditions. Buffum [2], Silkowski and Hall [24] and more recently Hall and Ekici [12] used indeed a "coupled mode" approach which requires several resolutions of the flow equations on each isolated blade row to compute reflection and transmission coefficients which are then assembled together to model a posteriori the interaction between the rows. Multichorochronic boundary conditions require on the contrary only one computation which takes intrinsically into account the coupling between the blade rows. Such boundary conditions have been used either in the frequency domain with the Harmonic Balance Technique [5, 23] or in the time domain [16, 19]. The HBT however assumes a harmonic flow field in the *whole* spatial domain and requires large memory resources since several coupled steady problems are solved simultaneously. Although they benefit from acceleration techniques and are in this regard faster to converge, time domain simulations are preferred in this paper since they are more accurate with respect to the hypothesis on the flow field.

We focus in this paper on this last type of simulation with an application to an industrial configuration of a vibrating contrafan. The numerical model of the fluid and the structure is first described in section 2. The multichorochronic boundary conditions are then detailed in section 3 in the case of single or multiple perturbations propagated through the boundaries. Finally the aeroelastic response computed with the full annulus model is analyzed in term of spectral content and the influence of several numerical parameters of the multichorochronic approximation is investigated in section 4. It is shown that a good agreement is found with respect to full annulus computations using only a small number of spinning modes (*i. e.* frequencies) for the approximation of the flow field with multichorochronic boundary conditions.

## 2 Numerical Model

### 2.1 Flow Model

Because of the relative motion of the different blade rows and their interactions, the significant role of viscous and turbulent effects and the deformation of the structure, the flow is governed by the Unsteady Reynolds Averaged Navier-Stokes (URANS) equations using the arbitrary Lagrangian-Eulerian formulation such that the deformation of the spatial domain $\mathscr{D}_F(t)$ induced by the flexible structure at the fluid-structure interface is taken into account. The equations are written in the relative frame of reference associated to the rigid body rotation of each blade row around the axis $\boldsymbol{i}_x$ at the constant rotation speed $\Omega$. Expressing the equations with the relative velocity components $\boldsymbol{v} = \boldsymbol{v}_{\text{abs}} - \boldsymbol{v}_{\text{rb}}$ leads finally to:

$$\frac{\mathrm{d}}{\mathrm{d}t}\int_{\mathscr{D}_F} \rho \,\mathrm{d}v + \oint_{\partial\mathscr{D}_F} \rho\,(\boldsymbol{v} - \boldsymbol{v}_d)\cdot\,\boldsymbol{n}\,\mathrm{d}s = 0, \tag{1a}$$

$$\frac{\mathrm{d}}{\mathrm{d}t}\int_{\mathscr{D}_F}\rho\boldsymbol{v}\,\mathrm{d}v+\oint_{\partial\mathscr{D}_F}[\rho\boldsymbol{v}\otimes(\boldsymbol{v}-\boldsymbol{v}_d)+p^\star\mathbf{I}]\,\boldsymbol{n}\,\mathrm{d}s=\oint_{\partial\mathscr{D}_F}\boldsymbol{\tau}^\star\boldsymbol{n}\,\mathrm{d}s+\int_{\mathscr{D}_F}\rho\,(\boldsymbol{f}_{\mathrm{Cor}}+\boldsymbol{f}_{\mathrm{cen}})\,\mathrm{d}v, \tag{1b}$$

$$\frac{\mathrm{d}}{\mathrm{d}t}\int_{\mathscr{D}_F}\rho E_r^\star\,\mathrm{d}v+\oint_{\partial\mathscr{D}_F}[\rho E_r^\star(\boldsymbol{v}-\boldsymbol{v}_d)+p^\star\boldsymbol{v}]\cdot\boldsymbol{n}\,\mathrm{d}s=\oint_{\partial\mathscr{D}_F}[\boldsymbol{\tau}^\star\boldsymbol{v}-\mathbf{q}^\star]\cdot\boldsymbol{n}\,\mathrm{d}s+\int_{\mathscr{D}_F}\rho\,\boldsymbol{v}\cdot\boldsymbol{f}_{\mathrm{cen}}\,\mathrm{d}v\,. \tag{1c}$$

The fluid is described by the density $\rho$, the momentum $\rho\boldsymbol{v}$ and the total energy $\rho E_r^\star$. The convective and diffusive fluxes are integrated on the domain boundary $\partial\mathscr{D}_F$ with the normal $\boldsymbol{n}$. The deformation of the fluid-structure interface is propagated in the spatial domain $\mathscr{D}_F$ using a structural analogy and induces a mesh deformation velocity $\boldsymbol{v}_d$ which modifies the convective fluxes. The rigid body motion produces the gyroscopic centrifugal and Coriolis forces $\boldsymbol{f}_{\mathrm{cen}}=-\partial\boldsymbol{v}_{\mathrm{rb}}/\partial t-\boldsymbol{\omega}\wedge\boldsymbol{v}_{\mathrm{rb}}$ and $\boldsymbol{f}_{\mathrm{Cor}}=-2\,\boldsymbol{\omega}\wedge\boldsymbol{v}$. For a rotating blade row, the angular velocity vector is $\boldsymbol{\omega}=\Omega\boldsymbol{i}_x$ and the rigid body velocity is $\boldsymbol{v}_{\mathrm{rb}}=\boldsymbol{\omega}\wedge r\boldsymbol{i}_r(\theta)=\Omega r\boldsymbol{i}_\theta(\theta)$ with $(r,\theta)$ the cylindrical coordinates in the relative frame. The centrifugal force finally reduces to $\boldsymbol{f}_{\mathrm{cen}}=\Omega^2 r\boldsymbol{i}_r(\theta)$.

The starred quantities $p^\star=p+2/3\,k_t$, $E_r^\star=E_r+k_t=e+\|\boldsymbol{v}\|/2+k_t$, $\boldsymbol{\tau}^\star=(1+\mu_t/\mu)\boldsymbol{\tau}$ and $\mathbf{q}^\star=(1+\mu_t/\mu\,\mathrm{Pr}/\mathrm{Pr}_t)\mathbf{q}$ are defined from the turbulent kinetic energy $k_t$, the turbulent viscosity $\mu_t$ and the turbulent Prandtl number $\mathrm{Pr}_t=0.9$ if the Boussinesq's hypothesis is considered to model turbulent effects. The heat flux is given by the Fourier law $\mathbf{q}=-k_T\nabla T$ based on the heat conductivity $k_T$. The stress tensor for a Newtonian fluid is $\boldsymbol{\tau}=-2/3\mu\,(\mathrm{div}\,\boldsymbol{v})\,\mathbf{I}+\mu(\nabla\boldsymbol{v}+(\nabla\boldsymbol{v})^{\mathsf{T}})$ with the Stokes hypothesis. For a perfect gas, the internal energy and the pressure are given by $e=c_vT$ and $p=\rho R_sT$ where $R_s$ is the specific constant and the specific heat ratio $\gamma=c_p/c_v$ is constant. The viscosity is governed by the Sutherland law $\mu(T)=\mu_S\sqrt{T/T_S}(1+C_S/T_S)/(1+C_S/T)$ and the heat conductivity is $k_T=c_p\mu/\mathrm{Pr}$. The one-equation Spalart-Allmaras model [26] is considered in this paper and the vector of flow variables is therefore $\boldsymbol{w}=\rho\,[1,\boldsymbol{v},E_r^\star,\tilde{\nu}]^{\mathsf{T}}$ with $\tilde{\nu}=\nu_t=\mu_t/\rho$ far from the walls. The turbulent kinetic energy is thus neglected in the approximation of $p^\star$ and $E_r^\star$.

Adiabatic wall boundary conditions are applied on the hub, the carter and the blade surfaces. The kinematics imposes that the absolute velocity match the wall velocity $\boldsymbol{v}_{\mathrm{abs}}=\boldsymbol{v}_w$ and the condition on the relative velocity thus writes $\boldsymbol{v}=\boldsymbol{v}_w-\boldsymbol{v}_{\mathrm{rb}}$. The wall velocity for the blades is $\boldsymbol{v}_w=\boldsymbol{v}_{\mathrm{rb}}+\boldsymbol{v}_d$ since they are rotating and deformable, hence the condition $\boldsymbol{v}_{\mathrm{blades}}=\boldsymbol{v}_d$. On the contrary the hub rotates rigidly, so the condition writes $\boldsymbol{v}_{\mathrm{hub}}=\mathbf{0}$. Finally the carter is a fixed surface in the absolute frame and is rigid; the wall velocity is $\boldsymbol{v}_w=\mathbf{0}$ and the relative velocity has to satisfy $\boldsymbol{v}_{\mathrm{carter}}=-\boldsymbol{v}_{\mathrm{rb}}$. An additional condition on the temperature $T=T_w$ is also taken into account.

A subsonic injection boundary condition is prescribed on the inlet plane where the field values are determined from prescribed values of the stagnation pressure and enthalpy, the direction of the velocity vector and a characteristic relation. On the outlet plane, a subsonic pressure condition is applied when computations are performed on a radial slice of the 3D model. Otherwise a valve boundary condition is imposed on the 3D model's outlet plane such that a target pressure and massflow are simultaneously prescribed at a given radial position. This condition is then supplemented by a radial equilibrium condition to define the pressure along the radial direction. Full annulus 360° simulations use matching joins on the azimuthal boundaries of each passage and a sliding plane boundary condition is applied at the interface between the blade rows. On the contrary, single passage simulations require multichorochronic boundary conditions on these boundaries to link the flow field appropriately. Such

boundaries are described more thoroughly in section 3.

The flow equations are discretized with a Finite Volume technique. The fluxes are approximated by the 2nd order Roe's scheme with Van Albada's limiter and Harten entropic correction. The time integration combines the implicit backward Euler scheme and the 2nd order Gear's method which solves the subiterations in physical time-step unlike the Dual Time Stepping. See [3] for more details about the CFD solver.

### 2.2 Structural Model

The structural domain $\mathscr{D}_S = \bigcup_{k=0}^{N_b-1} B_k$ is assumed to be made up of $N_b$ tuned blades $B_k$ which are identical to the reference blade $B_0$ through a rotation of the pitch angle $\beta = 2\pi/N_b$. The cyclic symmetry of such structures thus induces a spatial periodicity of the solution which can be reduced on a single blade passage based on physical considerations [7, 18]. More recently and from a mathematical point of view, the assumption of a Fourier decomposition of the mechanical variables has led to properly set the variational formulation of the problem [30]. The physical displacements on any blade $B_k$ consequently write as the sum of $N_b$ traveling wave coordinates $\boldsymbol{u}_{n_d}$

$$\boldsymbol{u}(B_k,t) = \Re\left\{\sum_{n_d=0}^{N_b-1} \boldsymbol{u}_{n_d}(B_k,t)\right\}. \tag{2}$$

Each traveling wave coordinate $\boldsymbol{u}_{n_d}$ satisfies the so-called cyclic symmetry boundary condition:

$$\boldsymbol{u}_{n_d}(B_k,t) = \boldsymbol{u}_{n_d}(B_0,t)\, e^{\mathrm{i}\, k\sigma_{n_d}} \tag{3}$$

with the following definition of the interblade phase angle (IBPA) $\sigma_{n_d}$ which characterizes the spatial phase shift between the displacements of the different blades

$$\sigma_{n_d} = n_d\, \beta = n_d \frac{2\pi}{N_b}. \tag{4}$$

The physical displacements on any blade $B_k$ are therefore known from the resolution of $N_b$ equations for each traveling wave coordinate computed only for the reference blade $B_0$ by combining Eqs. (2) and (3). For a linear elastic structure, the Finite Elements discretization supplemented by the cyclic symmetry boundary condition linking the lower ($L$) and upper ($U$) sides of the reference blade $B_0$ leads to the following system of equations for $n_d = 0, \ldots, N_b - 1$ using the same notations as [28]

$$\mathbf{M}\,\ddot{\boldsymbol{u}}_{n_d}(t) + \mathbf{C}\,\dot{\boldsymbol{u}}_{n_d}(t) + \mathbf{K}\,\boldsymbol{u}_{n_d}(t) = \boldsymbol{f}_{a,n_d}(\boldsymbol{u}_{n_d}, \dot{\boldsymbol{u}}_{n_d}) \tag{5a}$$

$$\boldsymbol{u}^L_{n_d}(t) = \boldsymbol{u}^U_{n_d}(t)\, e^{\mathrm{i}\,\sigma_{n_d}} \tag{5b}$$

where $\mathbf{M}$ is the mass matrix, $\mathbf{K}$ is the stiffness matrix including the centrifugal effects and $\mathbf{C}$ is the damping and gyroscopic effect matrix. The right-hand side of Eq. (5a) stands for the aerodynamic forces exerted by the pressure on the reference blade's fluid-structure interface $\Gamma_0$ with the assumption that the pressure field also satisfies the cyclic symmetry property ($p(B_k) = p(B_0)e^{\mathrm{i}k\sigma_{n_d}}$):

$$\boldsymbol{f}_{a,n_d}(\boldsymbol{u}_{n_d}, \dot{\boldsymbol{u}}_{n_d}) = \int_{\Gamma_0} p(B_0, \boldsymbol{u}_{n_d}, \dot{\boldsymbol{u}}_{n_d})\, \boldsymbol{n}\, \mathrm{d}s. \tag{6}$$

The vibratory behavior of the structure is described for small amplitudes of vibration by the eigenmodes which are the solution of the conservative part of Eq. (5a) with the additional constraint of cyclic symmetry:

$$\mathbf{K}\,\boldsymbol{\varphi}^{(i)}_{n_d} - \omega^{(i)2}_{n_d}\,\mathbf{M}\,\boldsymbol{\varphi}^{(i)}_{n_d} = \mathbf{0} \tag{7a}$$

$$\boldsymbol{\varphi}^{(i)L}_{n_d} = \boldsymbol{\varphi}^{(i)U}_{n_d}\, e^{\mathrm{i}\,\sigma_{n_d}}. \tag{7b}$$

Each mode type $\boldsymbol{\varphi}_{n_d}^{(i)}$ for $i = 1, \ldots, n_m$ has $N_b$ different spatial patterns corresponding to the nodal diameter $n_d = 0, \ldots, N_b - 1$. Because of the cyclic symmetry boundary condition, the modes are complex conjugates (except for $n_d = 0$ and $N_b/2$ if $N_b$ is even in which case the modes are real) and Eqs. (7) are therefore solved only for $n_d = 0, \ldots, \widetilde{N}_b$ with $\widetilde{N}_b = N_b/2$ if $N_b$ is even or $\widetilde{N}_b = (N_b - 1)/2$ if $N_b$ is odd. The remaining modes referred to by the index $-n_d$ are deduced by the conjugate relation $\boldsymbol{\varphi}_{-n_d}^{(i)} = \overline{\boldsymbol{\varphi}}_{n_d}^{(i)}$ and the eigenvalues are identical: $\omega_{-n_d}^{(i)} = \omega_{n_d}^{(i)}$. The eigenmodes inherit the cyclic symmetry property and are defined on any blade $B_k$ with the relation

$$\boldsymbol{\varphi}_{n_d}^{(i)}(B_k, t) = \boldsymbol{\varphi}_{n_d}^{(i)}(B_0, t)\, e^{\mathrm{i}\, k\sigma_{n_d}}. \tag{8}$$

Each traveling wave coordinate is finally approximated as a linear combination of the first eigenmodes and can be defined on any blade $B_k$ with Eq. (8):

$$\boldsymbol{u}_{n_d}(B_k, t) \approx \sum_{i=1}^{n_m} \boldsymbol{\varphi}_{n_d}^{(i)}(B_0)\, e^{\mathrm{i}\, k\sigma_{n_d}}\, q_{n_d}^{(i)}(t). \tag{9}$$

The present aeroelastic simulations are performed for a given modal shape and nodal diameter $\boldsymbol{\varphi} = \boldsymbol{\varphi}_{n_{d_0}}^{(i_0)}$ with a prescribed harmonic motion such that the generalized coordinate $q(t) = q_{n_{d_0}}^{(i_0)}(t)$ is defined with the eigenpulsation $\omega_{\mathrm{ael}} = \omega_{n_{d_0}}^{(i_0)}$ and the amplitude $q^*$. Using Eq. (2) for a single traveling wave $n_{d_0}$ and Eq. (9) with a single mode $i_0$, the physical displacement on any blade $B_k$ thus depends on the phase shift $\sigma_{\mathrm{ael}} = \sigma_{n_{d_0}}$ and reduces to:

$$\boldsymbol{u}_{\mathrm{pres}}(B_k, t) = \Re\Big\{ \boldsymbol{\varphi}(B_0)\, q^* e^{\mathrm{i}(k\sigma_{\mathrm{ael}} - \omega_{\mathrm{ael}}\, t)} \Big\}. \tag{10}$$

Such a displacement is a traveling wave coordinate $\boldsymbol{u}_{\mathrm{pres}} = \boldsymbol{u}_{n_{d_0}}$ and satisfies necessarily the cyclic symmetry boundary condition Eq. (5b). The time derivative of this prescribed motion defines the deformation velocity $\boldsymbol{s}_d(\Gamma, t) = \dot{\boldsymbol{u}}_{\mathrm{pres}}(\Gamma, t)$ of the fluid-structure interface $\Gamma$ which is used for the wall boundary condition of the fluid problem.

## 3 Multichorochronic Boundary Conditions

The structural equations of motion have been formulated in the previous section 2.2 on the reference blade domain only using the cyclic symmetry boundary condition Eq. (3). Similar boundary conditions known as (multi)chorochronic boundary conditions are now formulated for the flow domain so that single passage fluid-structure simulations are possible.

### 3.1 Chorochronicity for Blade Rows Interaction or Aeroelasticity

Chorochronic boundary conditions are used for single passage models to approximate flow perturbations induced by blade rows interactions in the case of a single stage or aeroelastic effects due to the vibration of an isolated blade row. The boundary condition assumes that the flow field vector $\boldsymbol{w}$ on the azimuthal boundaries of the passage can be related by chorochronic relations such that

$$\boldsymbol{w}(x, r, \theta - \beta, t) = \boldsymbol{w}(x, r, \theta, t - \tau) \tag{11}$$

with $\beta = 2\pi/N_b$ the pitch angle of the current blade row and $\tau$ the time phase-lag. These quantities are linked to the spatial wave number $\kappa$ and the pulsation of the unsteady phenomenon $\omega$ and define the phase shift $\sigma$ such that:

$$\sigma = \kappa\, \beta = \omega\, \tau. \tag{12}$$

### 3.1.1 Aeroelastic Excitation

Since the perturbation of the flow field stems from the displacement Eq. (10) prescribed to the blade with the nodal diameter $n_d$, the unsteady phenomenon is characterized by the wave number $\kappa = n_d$ and the eigenpulsation $\omega_{\text{ael}} = \omega_{n_d}^{(i)}$ of the structural mode considered. The phase $\sigma$ introduced in Eq. (12) is therefore just the IBPA defined in Eq. (4). According to the sign of the nodal diameter $n_d = 0, \ldots, \pm\widetilde{N}_b$ which is either positive or negative the following forward or backward time phase-shift is produced:

$$\tau_{n_d} = \frac{n_d\,\beta}{\omega_{\text{ael}}}. \tag{13}$$

The chorochronic boundary condition for aeroelasticity can be used for an isolated blade row and for a single nodal diameter only. The structural motion is therefore reduced to a single modal shape like in Eq. (10) for which the stability is evaluated.

The analogy between the cyclic symmetry boundary condition introduced in Eq. (5b) for the azimuthal boundaries of the structural passage and the chorochronic boundary introduced previously in Eq. (11) is clear if one consider that the lower (resp. upper) boundary is located at the azimuth $\theta - \beta$ (resp. $\theta$) and that a harmonic motion is prescribed to a single traveling wave coordinate. In this case Eq. (5b) (which is satisfied by the prescribed motion $\boldsymbol{u}_{\text{pres}}$) writes $\hat{\boldsymbol{u}}_{n_d}(\theta - \beta)e^{\mathrm{i}\omega_{\text{ael}}\,t} = \hat{\boldsymbol{u}}_{n_d}(\theta)e^{\mathrm{i}\omega_{\text{ael}}\,t}e^{\mathrm{i}\sigma_{n_d}}$; the right-hand side is re-arranged as $\hat{\boldsymbol{u}}_{n_d}(\theta)e^{\mathrm{i}\omega_{\text{ael}}}\,(t - \tau_{n_d})$ with the previous definition Eq. (13) of the time phase-lag and the cyclic symmetry boundary condition Eq. (5b) finally writes $\boldsymbol{u}_{n_d}(\theta - \beta, t) = \boldsymbol{u}_{n_d}(\theta, t - \tau_{n_d})$ which is essentially of the form Eq. (11).

### 3.1.2 Blade Rows Interaction

In the case of a single (rigid) stage, the flow field is perturbed by the unsteady fluctuations induced by the neighboring blade row. The pulsation of the unsteady phenomenon impinging on the current blade row with $N_b^{\text{cur}}$ blades now depends on the blade count $N_b^{\text{adj}}$ of the adjacent blade row and is given by

$$\omega_{\text{adj}\,>\,\text{cur}} = |N_b^{\text{adj}}\,\Delta\Omega| \tag{14}$$

with $\Delta\Omega = \Omega^{\text{adj}} - \Omega^{\text{cur}}$ the relative velocity between the blade rows. The wave number of the perturbation seen by the current blade row is $\kappa = N_b^{\text{adj}}$. From the previous definitions of the phase-shift Eq. (12), the time phase-lag is

$$\tau_{\text{adj}\,>\,\text{cur}} = \frac{N_b^{\text{adj}}\;\beta^{\text{cur}}}{\omega_{\text{adj}\,>\,\text{cur}}} = \frac{\beta^{\text{cur}}}{\Delta\Omega}. \tag{15}$$

The pulsation is zero if $\Delta\Omega = 0$, that is if the two blade rows have the same velocity. For such stages the flow is steady and chorochronic boundary conditions are unnecessary since there is no relative unsteady motion. For multistage configurations like a stator/rotor/stator configuration this steady contribution arising from the interaction between the stators cannot be propagated correctly using chorochronic boundary conditions since the time phase-lag would be infinite. This clocking effect described for example in [4] can lead to continuity and conservation losses. More advanced chorochronic boundary conditions are currently being developed [27] to take such phenomena into account.

Table 1 summarizes the values of the parameters involved in the definition of mono-periodic chorochronic boundary conditions for aeroelastic and blade rows interactions.

## 3.2 Multichorochronic Boundary Conditions for Multiple Input

When multiple sources of perturbation are experienced by a blade row, the chorochronic boundary condition has to be extended to deal with several frequencies and time phase-lags. We assume that the flow field *on the azimuthal*

| Simulation type | $\kappa$ | $\beta$ | $\omega$ | $\tau$ | $\sigma$ |
|---|---|---|---|---|---|
| Aeroelastic, nodal diam. $n_d$, pulsation $\omega_{\text{ael}}$, isolated row | $n_d$ | $2\pi/N_b$ | $\omega_{\text{ael}}$ | $\dfrac{n_d\beta}{\omega_{\text{ael}}}$ | $n_d\beta$ |
| Single stage, rigid blades, relative velocity $\Delta\Omega$ | $N_b^{\text{adj}}$ | $2\pi/N_b^{\text{cur}}$ | $N_b^{\text{adj}}\,\Delta\Omega$ | $\dfrac{\beta}{\Delta\Omega}$ | $N_b^{\text{adj}}\,\beta$ |

**Table 1**: Summary of wave parameters for chorochronic boundary conditions.

*boundaries of the passage only* can be decomposed as the sum of several perturbations according to the spinning mode theory of Tyler and Soffrin [29]. Each perturbation, or spinning mode, is a harmonic oscillation at a given frequency $\omega_p$ and wave number $\kappa_p$ such that [13]

$$\boldsymbol{w}(x,r,\theta,t) = \boldsymbol{w}_0(x,r,\theta) + \sum_{p=1}^{N_{\text{sp}}} \boldsymbol{w}_p(x,r,\theta,t) \tag{16}$$

with the following phase shift associated to each spinning mode

$$\sigma_p = \kappa_p\beta = \omega_p\tau_p. \tag{17}$$

In practice, the flow field is approximated with a Fourier decomposition using $N_{h,p}$ harmonics such that each spinning mode writes

$$\boldsymbol{w}_p(x,r,\theta,t) = \sum_{k=1}^{N_{h,p}} \boldsymbol{w}_{p,k}(x,r,\theta,t) = \sum_{k=1}^{N_{h,p}} \Re\Big\{\boldsymbol{c}_{p,k}(x,r)e^{\mathrm{i}k(\omega_p t + \kappa_p\theta)}\Big\}. \tag{18}$$

The Fourier coefficients $\boldsymbol{c}_{p,k}^U$ and $\boldsymbol{c}_{p,k}^L$ are computed on upper and lower azimuthal boundaries, *i. e.* for a given value of the angle $\theta^U$ and $\theta^L$ distant from $\beta$. The flow field on each boundary is then updated by means of characteristics relations which determine the boundary to update with respect to the flux in the opposite one. Assuming without loss of generality that the lower boundary has to be updated, the boundary condition imposes for each harmonic that $\boldsymbol{c}_{p,k}^L = \boldsymbol{c}_{p,k}^U$ and the flow field is easily deduced from the Fourier coefficients computed on the upper boundary using Eq. (18):

$$\begin{aligned}
\boldsymbol{w}_{p,k}^L(x,r,\theta^L,t) &= \Re\Big\{\boldsymbol{c}_{p,k}^U(x,r)e^{\mathrm{i}k\left(\omega_p t + \kappa_p\theta^U - \kappa_p\beta\right)}\Big\} \\
&= \Re\Big\{\boldsymbol{c}_{p,k}^U(x,r)e^{\mathrm{i}k\left[\omega_p(t-\tau_p) + \kappa_p\theta^U\right]}\Big\} \\
&= \boldsymbol{w}_{p,k}^U(x,r,\theta^U,t-\tau_p).
\end{aligned} \tag{19}$$

Each harmonic of a given spinning mode in Eq. (18) thus satisfies the chorochronic boundary condition Eq. (19) with the same time shift $\tau_p$. The chorochronic boundary condition is consequently also verified by any spinning mode:

$$\boldsymbol{w}_p(x,r,\theta-\beta,t) = \boldsymbol{w}_p(x,r,\theta,t-\tau_p). \tag{20}$$

In the absence of any steady spatial distortion, the mean field $\boldsymbol{w}_0(x,r,\theta)$ has a spatial periodicity associated to the current blade count and can be written

$$\boldsymbol{w}_0(x,r,\theta) = \sum_{\ell=0}^{M_h} \Re\Big\{\widehat{\boldsymbol{c}_{0,\ell}}(x,r)e^{\mathrm{i}\ell N_b\theta}\Big\}. \tag{21}$$

The mean flow field is consequently identical on lower and upper azimuthal boundaries at $\theta^U$ and $\theta^L$ since $e^{\mathrm{i}\ell N_b\theta^L} = e^{\mathrm{i}\ell N_b\theta^U}e^{-\mathrm{i}\ell N_b\beta} = e^{\mathrm{i}\ell N_b\theta^U}$. This property can be used to interpret the mean part $\boldsymbol{w}_0(x,r,\theta)$ as a zeroth harmonic of the Fourier decomposition Eq. (18) which is rewritten as:

$$\boldsymbol{w}(x,r,\theta,t) = \sum_{p=1}^{N_{\text{sp}}}\sum_{k=0}^{N_{h,p}} \Re\Big\{\boldsymbol{c}_{p,k}(x,r)e^{\mathrm{i}k(\omega_p t + \kappa_p\theta)}\Big\}. \tag{22}$$

This implies that

$$\boldsymbol{c}_{p,0}(x,r) = \frac{\boldsymbol{w}_0(x,r,\theta)}{N_{\mathrm{sp}}} = \frac{1}{N_{\mathrm{sp}}} \sum_{\ell=0}^{M_h} \widehat{\boldsymbol{c}_{0,\ell}}(x,r) e^{\mathrm{i}\ell N_b \theta}. \tag{23}$$

The previous expressions are well defined only for discrete values of the azimuth $\theta = \theta^U, \theta^L$ or more generally $\theta = \theta_0 + m\beta$ with $m \in \mathbb{Z}$ in which case the mean part $\boldsymbol{w}_0$ does actually not depend on $\theta$ because of the periodicity postulated in Eq. (21). For the zeroth harmonic there is no phase-lag and the chorochronic relation Eq. (19) degenerates into $\boldsymbol{w}^L_{p,0}(x,r,\theta^L,t) = \boldsymbol{w}^U_{p,0}(x,r,\theta^U,t)$.

The Fourier coefficients are computed by means of the moving average technique adapted from [9, 13] to handle multiple frequencies. The coefficients are updated continuously at each time step until they reach a converged value. The stability of the computations strongly depends on the update of the coefficients and an under relaxation $\boldsymbol{c}^{t+\delta t}_{p,k} = (1-\eta_{p,k})\boldsymbol{c}^{t}_{p,k} + \eta_{p,k}\,\boldsymbol{c}^{t+\delta t}_{p,k}$ with $0 \leq \eta_{p,k} \leq 1$ is often necessary [15]. A low value of the relaxation parameter $\eta_{p,k} = 0.1$ is set by default to ensure a robust convergence and can be tuned for each spinning mode and each harmonic.

The multichorochronic hypothesis actually assumes that the flow field on the azimuthal boundaries is a linear superposition of different unsteady phenomena. The aeroelastic vibration and blade row interaction phenomena described previously can both be taken into account as a superposition of two primary spinning modes. Nonlinear effects arising from the interaction between the primary unsteady phenomena appear as additional spinning modes with linear combinations of the primary spinning modes' frequencies and wave numbers. Such spinning modes will be referred to secondary spinning modes later in the document. The level of approximation of the flow field on azimuthal boundaries thus depends on the number $N_{\mathrm{sp}}$ of spinning modes introduced and their relevance with respect to the physics. Although the inclusion of the primary spinning modes in the approximation is obvious, this is not the case for secondary spinning modes which contribute more or less according to the prescribed pattern of motion, to the operating point,... Since the secondary spinning modes involved are a priori unknown, we restrict ourselves in the simulations to the primary spinning modes and investigate the effects of the inclusion of the very first secondary spinning modes identified from full annulus computations.

### 3.3 Spinning Modes Definition in a Vibrating Contrafan

The vibration frequency $\omega_{\mathrm{ael}}$ has to be shifted if the perturbation induced by the structural deformation is observed in another relative frame (*i. e.* in another blade row) but the one in which the vibration is prescribed. The spinning mode relative to the vibration indeed writes $\boldsymbol{w}_p(x,r,\theta,t) = \sum_k \Re\{\boldsymbol{c}_{p,k}(x,r)e^{\mathrm{i}k(\omega_{\mathrm{ael}}t + n_d\theta)}\}$ but if the same mode is observed in another frame of reference such that the azimuth is given by $\theta' = \theta - \Delta\Omega t$, the spinning mode becomes $\boldsymbol{w}_p(x,r,\theta',t) = \sum_k \Re\{\boldsymbol{c}_{p,k}(x,r)e^{\mathrm{i}k[\omega_{\mathrm{ael}}t + n_d(\theta' + \Delta\Omega t)]}\}$, hence the frequency shift $\widetilde{\omega}_{\mathrm{ael}} = \omega_{\mathrm{ael}} + n_d\Delta\Omega$.

Besides the (shifted) vibration and blade passing frequencies associated to the primary spinning modes mentioned in section 3.1, the flow field can exhibit frequency combinations related to the secondary spinning modes which characterize nonlinear interactions of the primary unsteady phenomena. This mechanism of interaction and the Doppler effect induced by the change of relative frame has been explained by Silkowski and Hall [24] in the framework of the linearized Euler equations for aeroelasticity.

We propose here the following general expressions of the frequencies and wave numbers defining the different types of spinning modes involved in the flow field resulting from the interaction between the vibration of the structure with a prescribed nodal diameter and the blade passage effects induced by a

single adjacent blade row:

$$\omega_p = \omega(m,n) = \left| m\widetilde{\omega}_{\text{ael}} + n\omega_{\text{adj}\,>\,\text{cur}} \right|, \tag{24a}$$

$$\kappa_p = \kappa(m,n) = m\,n_d + n\,N_b^{\text{adj}} \tag{24b}$$

with the shifted vibration frequency

$$\widetilde{\omega}_{\text{ael}} = |\omega_{\text{ael}} + \chi_{\text{ael}} n_d\,\Delta\Omega|. \tag{25}$$

The indicator function $\chi_{\text{ael}}$ is equal to 0 if the spinning modes are defined in the relative frame of the vibrating blade row and is equal to 1 in other relative frames to take into account the Doppler effect. The definitions of the blade passing frequency $\omega_{\text{adj}\,>\,\text{cur}}$ and of the relative velocity $\Delta\Omega$ are those given in section 3.1.2.

To sum up, the spinning modes are completely defined by the pair of integers $(m,n) \in \mathbb{Z}\times\mathbb{Z}$ using the relations Eqs. (24) and (25), the number of harmonics $N_{h,p}$ for each spinning mode and the list of relaxation parameters $\eta_{p,k}$ for the update of the Fourier coefficients. The flow field on the boundaries is therefore approximated by a set of spinning modes $\mathcal{SP} = \{(m,n) \in E \subset \mathbb{Z}\times\mathbb{Z}\}$ such that $\text{card}(\mathcal{SP}) = N_{\text{sp}}$; the subset $E$ is selected a priori and contains at least the pairs $(1,0)$ and $(0,1)$ corresponding to the primary spinning modes. Subsets of the spinning modes set $\mathcal{SP}$ can also be defined: the primary spinning modes set is defined by $\mathcal{SP}_1 = \{(1,0),(0,1)\}$ and corresponds to the vibration and the blade passage phenomena whereas the secondary spinning modes set is defined by $\mathcal{SP}_2 = \{(m,n) \in E_2 \subset \mathbb{Z}^*\times\mathbb{Z}^*\}$ with $N_{\text{sp}}^k = \text{card}(\mathcal{SP}_k)$ and $N_{\text{sp}} = N_{\text{sp}}^1 + N_{\text{sp}}^2$. In practice the first harmonics only $(m,n) \in \{\pm1,\pm2\}^2$ are considered since the contribution of higher harmonics is often negligible [12, 24].

The previous description could be easily generalized in the case of $N_{\text{sp}}^1 > 2$ primary spinning modes and leads to the following definitions:

$$\omega_p = \omega(n_1,\ldots,n_{N_{\text{sp}}^1}) = \left| \sum_{m=1}^{N_{\text{sp}}^1} n_m\,\omega_{p,m} \right|, \tag{26a}$$

$$\kappa_p = \kappa(n_1,\ldots,n_{N_{\text{sp}}^1}) = \sum_{m=1}^{N_{\text{sp}}^1} n_m\,\kappa_{p,m} \tag{26b}$$

where the frequencies $\omega_{p,m}$ and wave numbers $\kappa_{p,m}$ are those associated to the primary spinning modes. One can then define the set $\mathcal{SP}_1$ containing all primary spinning modes and $N_{\text{sp}}^1 - 1$ other subsets of interacting spinning modes $\mathcal{SP}_k$ such that:

$$\mathcal{SP}_1 = \{(n_1,\ldots,n_{N_{\text{sp}}^1}) | \exists! i \in D \text{ s.t. } n_i = 1, n_j = 0 \text{ if } i \neq j\}, \tag{27a}$$

$$\mathcal{SP}_k = \{(n_1,\ldots,n_{N_{\text{sp}}^1}) \in E_k\} \text{ for } k = 2,\ldots,N_{\text{sp}}^0, \tag{27b}$$

$$E_k \subset \{(m_1,\ldots,m_{N_{\text{sp}}^1}) | \exists F = \{e_1,\ldots,e_k\}, e_k \neq e_l \text{ for } k \neq l, e_k \in D,$$
$$\text{s.t. } m_i \in \mathbb{Z}^* \text{ for } i \in F, m_j = 0 \text{ for } j \in D \setminus F\}, \tag{27c}$$

$$D = \{i \in \mathbb{N}, 1 \leq i \leq N_{\text{sp}}^1\}. \tag{27d}$$

$$\mathcal{SP} = \bigcup_{k=1}^{N_{\text{sp}}^1} \mathcal{SP}_k \text{ with } N_{\text{sp}} = \text{card}(\mathcal{SP}) = \sum_{k=1}^{N_{\text{sp}}^1} N_{\text{sp}}^k \tag{27e}$$

As an example if the two blades were vibrating, one would have $N_{\text{sp}}^1 = 3$ with $\omega_{p,m} \in \{\omega_{\text{ael}}^{(1)}, \omega_{\text{adj}\,>\,\text{cur}}, \omega_{\text{ael}}^{(2)}\}$ and $\kappa_{p,m} \in \{n_d^{(1)}, N_b^{\text{adj}}, n_d^{(2)}\}$. The set of primary spinning modes would be $\mathcal{SP}_1 = \{(1,0,0),(0,1,0),(0,0,1)\}$ and the secondary and tertiary sets of spinning modes could be $\mathcal{SP}_2 = \{(1,1,0),(0,1,1),(1,0,1)\}$ and $\mathcal{SP}_3 = \{(1,1,1),(1,-1,1),(1,1,-1)\}$, hence a total number of spinning modes $N_{\text{sp}} = 9$.

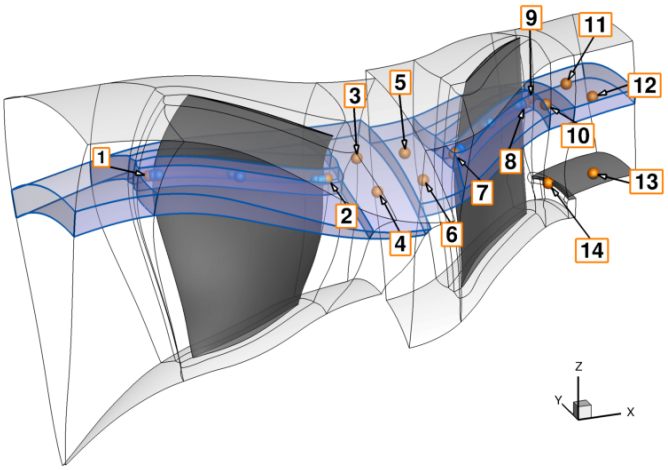


**Figure 1**: Single passage configurations of the contrafan. The 2.5D model is represented with the blue slice. The monitoring points for pressure time histories are plotted with orange and blue spheres.

**Table 2**: Geometrical parameters of the contrafan.

| Parameter | $R_0$ | $R_1$ |
|---|---|---|
| Blade count $N_{b,i}$ [-] | 10 | 14 |
| Chord [mm] | 118 | 105 |
| Gap-to-chord ratio [%] | 0.36 | 0.31 |
| Stagger angle [°] | −47 | 47 |
| Rotation speed $\Omega_i$ [rpm] | $\Omega_0$ | $\Omega_1$ |

## 4 Results and Discussion

### 4.1 Configuration for 3D and 2.5D Models

Numerical results are presented for the VITAL ("enVIronmenTALly friendly aero-engine") contrafan designed as new engine architecture for noise and emission reduction [20]. The configuration is made up of two contra-rotating fans with $N_{b,0} = 10$ and $N_{b,1} = 14$ blades and a splitter downstream. The geometrical details of the configuration are given in table 2. Computations are performed at 70% of the nominal speed for an intermediate throttling.

The 3D single passage model contains about 4.2 millions of control cells. Computations are thus time consuming and a radial slice is extracted to work initially with a lighter 2.5D model. The extracted mesh represented on the figure 1 inside the whole 3D domain includes only 3 cells along the radial direction in the first row and 2 in the second row. The mesh does indeed not match on both sides of the interrow plane and the sliding nomatch boundary condition at the interface has to perform some 2D interpolations both in the radial and azimuthal directions.

Though the flow field computed with the 3D and 2.5D models is slightly different since the streamlines are artificially confined in the 2.5D model, the general agreement is quite good as one can see on figure 2 where the pressure field is compared. The main purpose of the 2.5D model is not to predict very

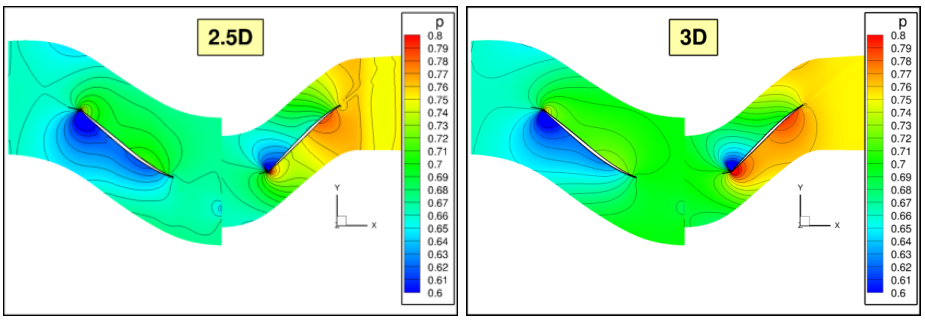


**Figure 2**: Comparison of steady pressure fields computed with the 2.5D and 3D models.

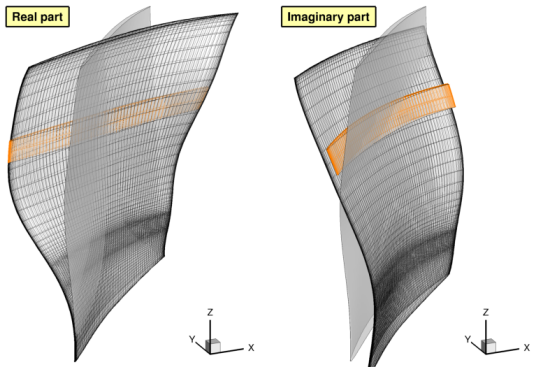


(a) 3D model, $n_d = 2$

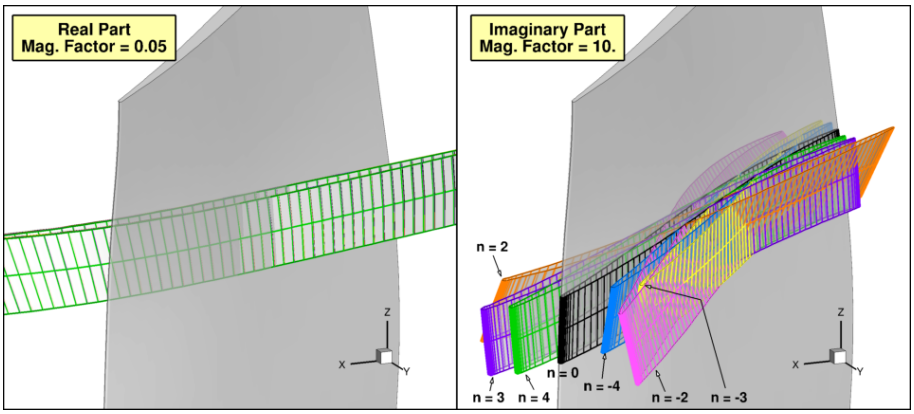


(b) 2.5D model, $n_d \in \{0, \pm1, \pm2, \pm3, \pm4\}$

**Figure 3**: Modal deformations of the first torsion mode for several nodal diameters.

accurately the physics but to compare computations on a single passage using multichorochronic boundary conditions with full annulus computations which can be performed in a reasonable time with this lighter model. Indeed, the full annulus 2.5D model contains less than 1 millions of cells (that is barely a quarter of the size of the 3D model on a single passage) whereas the full annulus 3D model would contain about 50 millions of cells.

Several monitoring points inside the fluid domain (14 points) and on the blades surfaces (8 points for each blade) are selected to check the time histories. Their location is represented by the orange and blue spheres on figure 1. For each blade two probes are located in the fluid domain near the leading and trailing edges; additional probes are also selected in the blocks on both sides of the interrow and in the wake of the second row. Wall pressure probes are distributed as follows on each blade surface: two probes at the leading and trailing edges, two additional probes near the leading / trailing edges and two other probes at the middle of the blade surfaces.

The flexibility of blade row $R_1$ is described by the 1$^{\text{st}}$ torsion mode for the nodal diameters $n_d \in \{0, \pm1, \pm2, \pm3, \pm4\}$. The eigenfrequency, which slightly depends on the nodal diameter, is about $\omega_{\text{ael}} = 545$ Hz. Pictures of figure 3 show the amplified real and imaginary parts of the deflections for the 3D model and the slices corresponding to the 2.5D model.

Preliminary simulations have been performed on the contrafan stage with rigid blades to check that both the 2.5D and 3D models capture well the blade passing frequencies given in section 3.1.2 with (multi)chorochronic boundary conditions. Aeroelastic computations have also been performed with (multi)chorochronic boundary conditions on the isolated blade row $R_1$. In both cases, the use of multichorochronic boundary conditions with only one spinning mode (corresponding either to the blade passage or the vibration) reproduces exactly the same time histories recorded by the different probes after the tran-

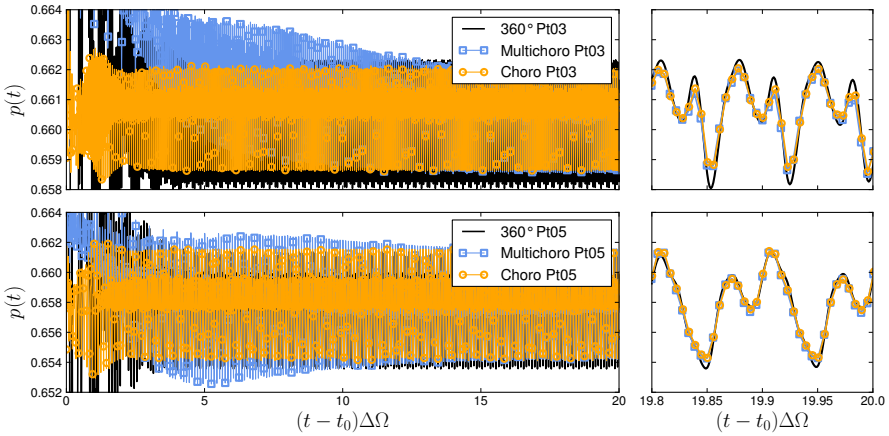


(a) Rigid stage

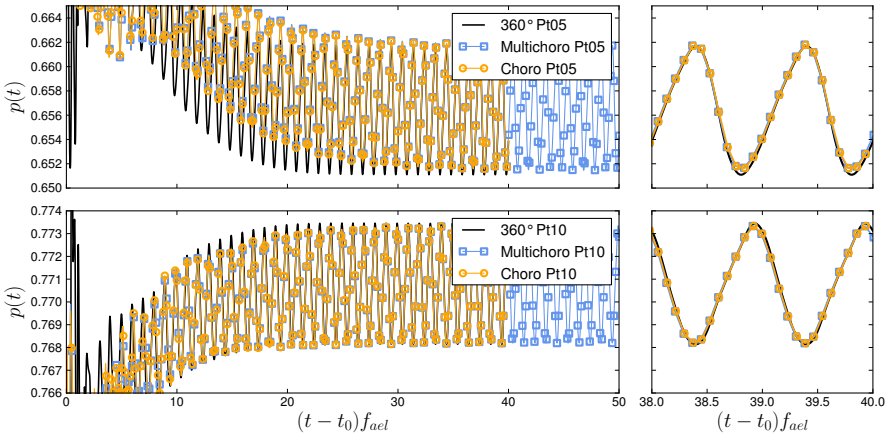


(b) Flexible isolated blade row

**Figure 4**: Comparison of pressure time histories computed with the 2.5D model on the full annulus and on a single passage using monochorochronic or multichorochronic boundary conditions with only one spinning mode.

sient has vanished. Figures 4a and 4b show the agreement between the different types of simulations.

The convergence with multichorochronic boundary conditions is longer because of the relaxation parameter $\eta$ used to update the Fourier coefficients. It is clearly visible from figure 4a that the convergence of the simulation for the rigid stage performed with $\eta = 0.1$ is far longer compared to the "classical" monochorochronic computation performed without any relaxation (*i. e.* $\eta = 1$). On the contrary, the aeroelastic simulation for the isolated blade row performed with $\eta = 0.9$ converges almost as quickly as the monochorochronic computation (see Fig. 4b).

The spectra of the times histories are compared on figures 5a and 5b for the two probes. The same peaks are identified from the computations with monochorochronic or multichorochronic boundary conditions. For the rigid stage the main frequencies are the fundamental blade passing frequency and its first harmonics: the perturbations seen by the probes in $R_0$ (like the point 03 *e. g.*) oscillate at $k\omega_{R_1>R_0} = kN_{b,1}\Delta\Omega = k \times 2668$ Hz with $k \in \mathbb{N}$ whereas the perturbations seen by the probes in $R_1$ (like the point 05 *e. g.*) oscillate at $k\omega_{R_0>R_1} = kN_{b,0}\Delta\Omega = k \times 1906$ Hz with $k \in \mathbb{N}$. For the flexible isolated row, the perturbations seen by the probes oscillate at $k\omega_{\text{ael}} = k \times 545$ Hz. Aeroelastic computations performed on the isolated blade row have shown from the analysis of the generalized aerodynamic forces that the contrafan is the least stable for the nodal diameter $n_d = -2$ (results are not shown here for conciseness).

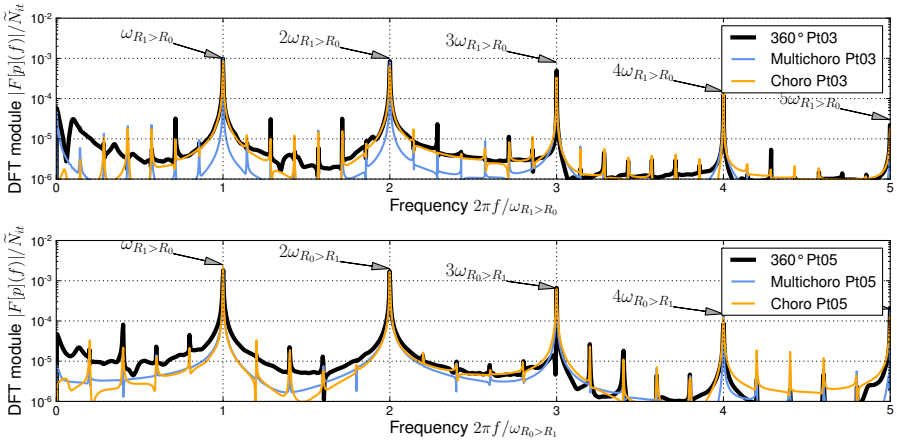


(a) Rigid stage

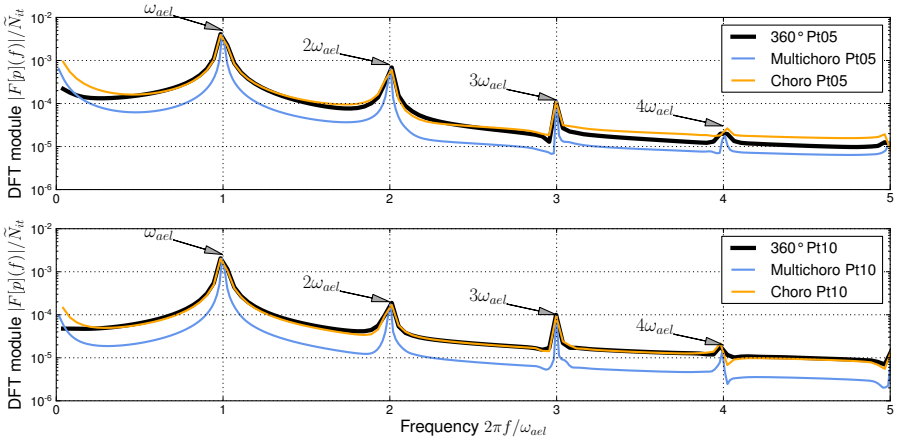


(b) Flexible isolated blade row

**Figure 5**: Comparison of pressure spectra for two probes computed with the 2.5D model on a single passage using monochorochronic or multichorochronic boundary conditions with only one spinning mode.

### 4.2 Full Annulus Computations

Full annulus computations are then performed on the stage configuration with a prescribed vibration on the second blade row. The objective is to check if the main spinning modes match up the first low harmonics of the combinations of frequencies described in section 3.3.

The time history of the probe 03 plotted on figure 6a clearly reveals the coexistence of at least two frequencies: the low vibration frequency $\omega_{\text{ael}}$ which is the most prominent and the blade passing frequency $\omega_{R_1>R_0}$ (and its harmonics) induced by the neighboring blade row $R_1$ which modulates the response with a lower magnitude. The trace of the vibration frequency in the time history of the different probes in $R_0$ highlights the significant influence of upstream traveling pressure waves, even for an amplitude of vibration as small as $q^* = 10^{-3}$. The maximal amplitude of the prescribed displacement Eq. (10) is therefore $\|\boldsymbol{u}_{\text{pres}}(B_0,t)\| = \max\{\varphi^{\Re}(\boldsymbol{x})q(t) + \varphi^{\Im}(\boldsymbol{x})q(t) \text{ for } (\boldsymbol{x},t) \in B_0 \times [0, 2\pi/\omega_{\text{ael}}]\} \sim 1$ mm, which is about 0.7% of the average blade height or about 3 times the tip gap height.

The time history of the probe 05 in $R_1$ plotted as an example on figure 6b is more erratic because of the complex interaction between the unsteady phenomena (wake due to $R_0$'s blade passage and vibration). The curve plotted in orange for comparison is the pressure time history computed for the isolated flexible row. It is dominated by the sole vibration frequency (and its harmonics) and produces a far more regular response which is periodic. An important point to notice here is that the forcing effect due to the wakes stemming from the first

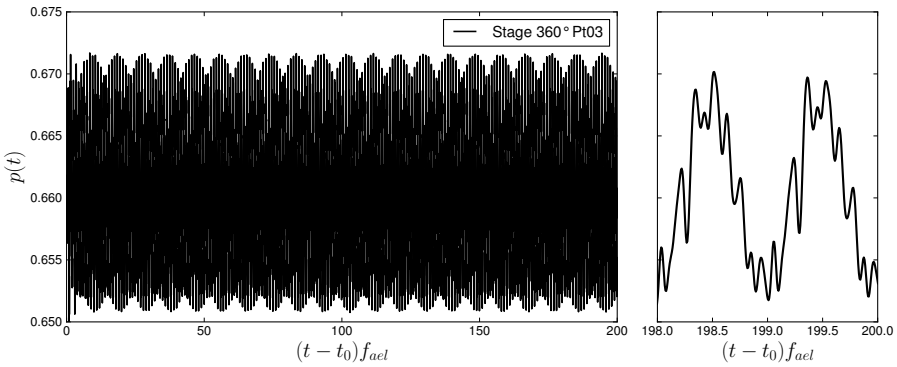


(a) Time history of probe 03 in $R_0$

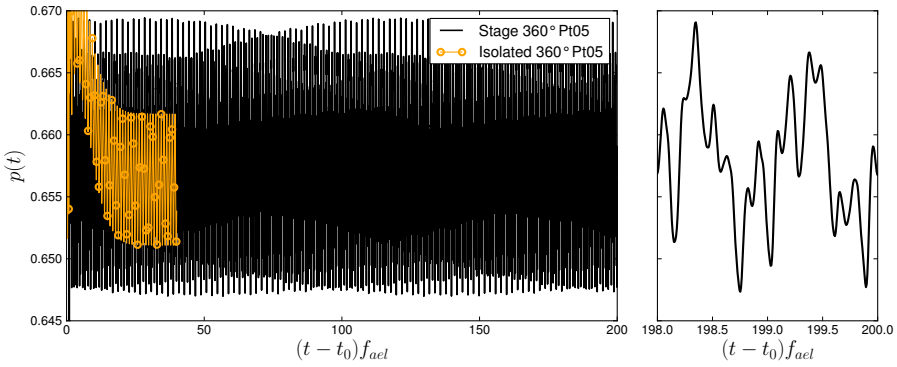


(b) Time history of probe 05 in $R_1$

**Figure 6**: Comparison of pressure time histories computed with the 2.5D model of the 360° flexible contrafan ($n_d = 0$, $q^* = 10^{-3}$).

blade row in the stage configuration clearly increases the pressure fluctuations in the second row, the envelope of the oscillations being almost doubled for the moderate amplitude of vibration considered.

We focus in the following on spectral analyses performed from the time histories in order to identify the main frequencies (and consequently the spinning modes) involved. We investigate briefly the influence of the amplitude and pattern of the prescribed vibration (this latter being defined for a particular nodal diameter) on the spectral contents of the pressure and generalized aerodynamic forces time histories.

The spectral analyses are performed for each probe in a same blade row. For each peak identified at a frequency $f_p$, an average magnitude is computed as $\overline{F}(f_p) = \sum_{k=1}^{N_{\text{probes}}} |F[p(P_k)](f_p)|/N_{\text{probes}}$ where $F[p(P_k)]$ is the module of the Fourier transform for the pressure recorded by the probe $P_k$. Peaks are identified in an interval ranging from the maximal average value $\overline{F}_{\max} = \max\{\overline{F}(f_p), p = 1, \ldots, N_{\text{peaks}}\}$ to $\varsigma\overline{F}_{\max}$ where $\varsigma$ typically equals 1%. The limits of this interval are represented by dashed gray lines on the plots and average peaks values are indicated by gray crosses. A quantity called spectral density indicator is finally defined as $S_d = \sum_{p=1}^{N_{\text{peaks}}} \overline{F}(f_p)/\overline{F}_{\max}$ on the interval of interest. The spectral density indicator of a periodic signal with a single peak is $S_d = 1$ but it increases when the magnitude of other peaks becomes significant. This quantity will therefore be used a simple indicator of the signal complexity.

### 4.2.1 Influence of the Amplitude of Vibration for $n_d = 0$

On figure 7a, the spectral analyses performed for each probe $P_k$ in $R_0$ highlight the most significant frequencies contributing to the pressure time histories. The main peaks are correlated to the spinning modes with respect to the frequencies identified. Following the description of section 3.3 and the definition Eq. (24a) of the pulsations associated to the spinning modes for the nodal diameter $n_d = 0$

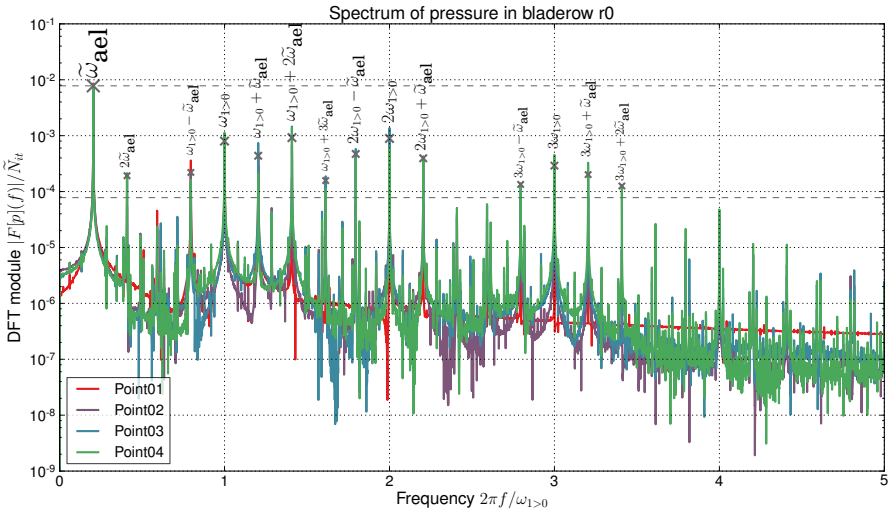


(a) Spectra of probes in $R_0$

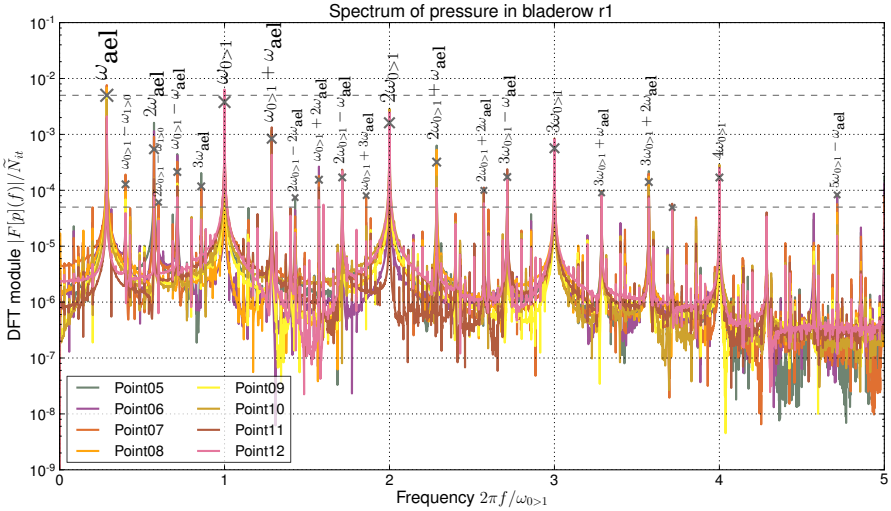


(b) Spectra of probes in $R_1$

**Figure 7**: Comparison of pressure spectra computed with the 2.5D model of the 360° flexible contrafan for the nodal diameter $n_d = 0$ and $q^* = 10^{-3}$.

considered here, it can be seen that the main spinning mode $(1, 0)$ is indeed due to the vibration with the pulsation $\widetilde{\omega}_{\text{ael}} = \omega_{\text{ael}}$. Amongst the other peaks with a magnitude greater than $\varsigma\overline{F}_{\max} = 0.01\,\overline{F}(f_{\text{ael}})$, one can identify the spinning modes associated to the blade passage and its harmonics $(0, 1)$, $(0, 2)$ and $(0, 3)$, but also some secondary spinning modes like $(\pm 1, n)$ with $n \in \{1, 2, 3\}$ which characterize the interaction between a harmonic of the blade passing frequency and the fundamental frequency of vibration. Additional interactions $(2, 1)$, $(3, 1)$ and $(2, 3)$ also contribute to the response. The spectral content of the different pressure time histories in $R_0$ can therefore be approximated with the set of primary spinning modes $\mathcal{SP}_1$ with few harmonics and with a set of secondary spinning modes $\mathcal{SP}_2$ comprising at least the family $(\pm 1, n)$ with $n \in \{1, 2, 3\}$.

The same analyses are performed for each probe $P_k$ in $R_1$ and the result is plotted on figure 7b. Here again the main spinning mode $(1, 0)$ corresponds to the vibration and its harmonics $(m, 0)$ for $m \in \{2, 3\}$ also contribute significantly, as well as the spinning mode associated to the blade passage and its harmonics $(0, n)$ for $n \in \{1, \ldots, 4\}$. The spectral density indicator $S_d$ is a bit higher for this blade row since the wakes convected downstream interact strongly with the vibration of the second blade row; the magnitudes of the peaks corresponding to the vibration $(1, 0)$ and the blade passage $(0, 1)$ are indeed of the

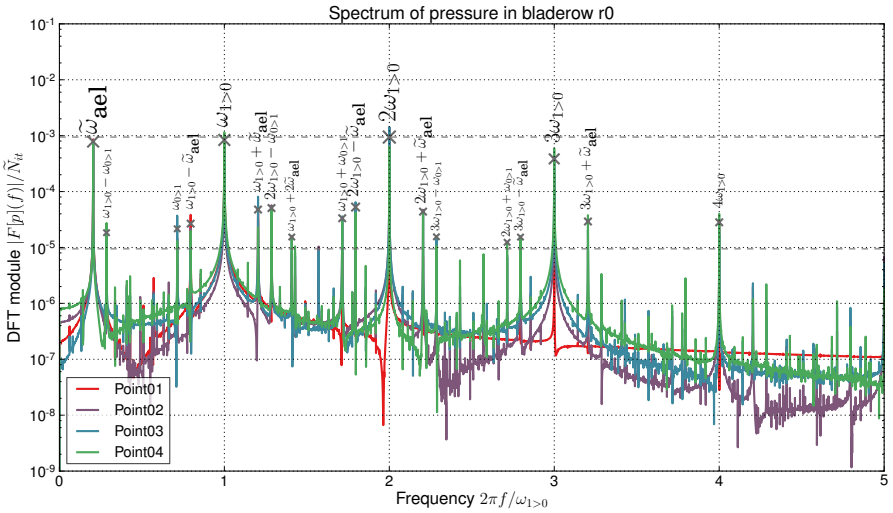


(a) Spectra of probes in $R_0$

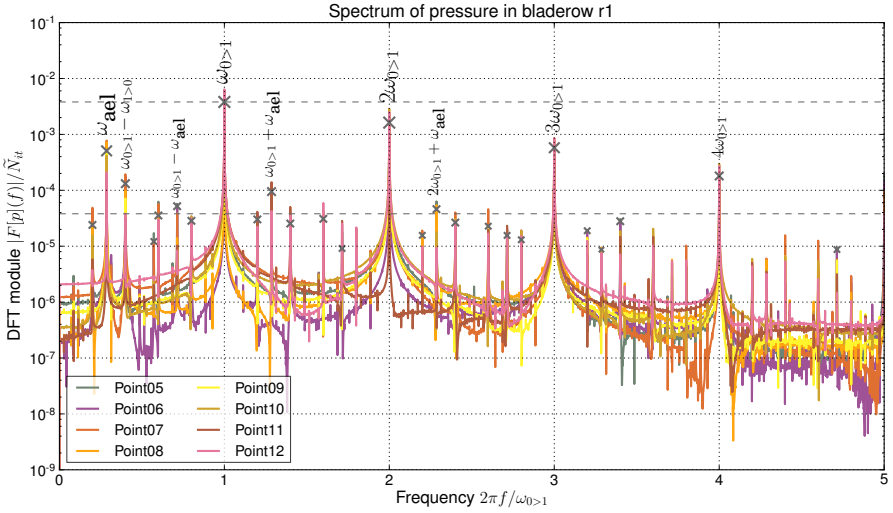


(b) Spectra of probes in $R_1$

**Figure 8**: Comparison of pressure spectra computed with the 2.5D model of the 360° flexible contrafan for the nodal diameter $n_d = 0$ and $q^* = 10^{-4}$.

same order. The majority of the other peaks identified are secondary spinning modes of the type $(\pm m, \pm n)$ for $m, n \in \{1, 2, 3\}$.

On can however notice the presence of other peaks which can be related to the interaction between the blade passing frequency of the adjacent blade row $\omega_{R_0>R_1}$ and the blade passing frequency of the current blade row $\omega_{R_1>R_0}$. These frequencies do not correspond to the spinning modes described by Eq. (24a) and cannot be interpreted with the interaction mechanism proposed by Silkowski and Hall [24]. One should therefore define $N^1_{\text{sp}} = 3$ primary perturbations with $\omega_{p,m} = \{\widetilde{\omega}_{\text{ael}}, \omega_{\text{adj}>\text{cur}}, \omega_{\text{cur}>\text{adj}}\}$ and use the more general definitions Eq. (26) to take these additional secondary spinning modes into account. In the present case the spinning modes $(0, 1, -1)$ and $(0, 2, -1)$ could be identified in this way. However their magnitude is very small compared to the main spinning mode corresponding here to the vibration and such spinning modes could be neglected.

The results of the spectral analyses performed for a smaller amplitude of vibration $q^* = 10^{-4}$ are plotted on figure 8. In the blade row $R_1$, the magnitude of the peaks due to the blade passage (spinning modes $(0, n)$ for $n \in \{1, \ldots, 4\}$) is unchanged since the perturbation due to the convection of the wakes downstream is not altered by changing the amplitude of vibration. However the magnitude of the peak associated to the vibration (spinning mode $(1, 0)$) is

| | $q^* = 10^{-4}$ | | $q^* = 10^{-3}$ | | $q^* = 2 \times 10^{-3}$ | |
|---|---|---|---|---|---|---|
| $R_0$ | $2\omega_{R_1>R_0}$ | :100% | $\widetilde{\omega}_{\text{ael}}$ | :100% | $\widetilde{\omega}_{\text{ael}}$ | :100% |
| | $\omega_{R_1>R_0}$ | : 89% | $\omega_{R_1>R_0} + 2\widetilde{\omega}_{\text{ael}}$ | : 12% | $\omega_{R_1>R_0} + 2\widetilde{\omega}_{\text{ael}}$ | : 22% |
| | $\widetilde{\omega}_{\text{ael}}$ | : 83% | $2\omega_{R_1>R_0}$ | : 11% | $\omega_{R_1>R_0}$ | : 6% |
| | $3\omega_{R_1>R_0}$ | : 41% | $\omega_{R_1>R_0}$ | : 10% | $\omega_{R_1>R_0} + 3\widetilde{\omega}_{\text{ael}}$ | : 5% |
| | $2\omega_{R_1>R_0} - \widetilde{\omega}_{\text{ael}}$ | : 6% | $2\omega_{R_1>R_0} - \widetilde{\omega}_{\text{ael}}$ | : 6% | $\omega_{R_1>R_0} + \widetilde{\omega}_{\text{ael}}$ | : 5% |
| | $S_d$ | : 3.6 | $S_d$ | : 1.7 | $S_d$ | : 1.7 |
| $R_1$ | $\omega_{R_0>R_1}$ | :100% | $\omega_{\text{ael}}$ | :100% | $\omega_{\text{ael}}$ | :100% |
| | $2\omega_{R_0>R_1}$ | : 43% | $\omega_{R_0>R_1}$ | : 76% | $\omega_{R_0>R_1}$ | : 38% |
| | $3\omega_{R_0>R_1}$ | : 15% | $2\omega_{R_0>R_1}$ | : 32% | $2\omega_{\text{ael}}$ | : 20% |
| | $\omega_{\text{ael}}$ | : 13% | $\omega_{R_0>R_1} + \omega_{\text{ael}}$ | : 17% | $2\omega_{R_0>R_1}$ | : 16% |
| | $4\omega_{R_1>R_0}$ | : 5% | $3\omega_{R_0>R_1}$ | : 11% | $\omega_{R_0>R_1} + \omega_{\text{ael}}$ | : 15% |
| | $S_d$ | : 1.9 | $S_d$ | : 2.9 | $S_d$ | : 2.5 |

**Table 3**: Relative magnitude of the 5 most significant peaks in the spectral analysis of pressure time histories for different amplitudes of vibration.

clearly smaller since it is directly related to the amplitude of vibration[1]. This results in a weaker spectral density for the blade row $R_1$: the contribution of the vibration is less pronounced and the response is dominated by the blade passing effect. In the blade row $R_0$, the magnitude of the peak due to vibration also decreases linearly with the vibration amplitude $q^*$. In this case however the magnitude associated to the spinning mode $(1, 0)$ corresponding to the vibration on one hand and to the spinning mode $(0, n)$ for $n \in \{1, 2, 3\}$ associated to the blade passage on the other hand are now of the same order. This induces more complicated interactions between the two phenomena than those observed in the case $q^* = 10^{-3}$ for this blade row, with the appearance of frequency combinations involving $\omega_{R_0>R_1}$ and $\omega_{R_1>R_0}$. For extremely small amplitudes of vibration the spectra would asymptotically converge to the rigid case in the limit $q^* \to 0$ (see Figure 5a) since the magnitude of the peak associated to the vibration would drop to zero.

For higher amplitudes of excitation, the vibration peak magnitude would dominate. However an intensification of nonlinear effects is expected and the spectral content could become extremely dense but the modal approximation would no longer be valid. Table 3 summarizes the relative magnitudes of the 5 main peaks identified for different amplitudes of vibration. The spectral density indicator is clearly larger when both the vibration and the blade passing effects produce perturbations with similar magnitudes. This is the case in blade row $R_0$ for $q^* = 10^{-4}$ and in blade row $R_1$ for $q^* = 10^{-3}$ as explained previously. An important conclusion is that for moderate amplitudes of vibration, only a few spinning modes could be considered to approximate the spectral content for an excitation with the nodal diameter $n_d = 0$. The relative magnitudes listed in table 3 indicate that only the primary spinning modes contribute significantly ($\overline{F}(f_p)/\overline{F}_{\max} \geq 20$ %). For a more detailed approximation ($\overline{F}(f_p)/\overline{F}_{\max} \geq 10$ %) some secondary spinning modes could be considered, but in this case only the first harmonics $(\pm m, \pm n)$ such that $m, n \in \{1, 2\}$ are significant. It should finally be mentioned that the same type of spectral analysis have been performed for time histories of the relative Mach number and the entropy and reveal the same type of spinning modes involved.

### 4.2.2 Influence of the Nodal Diameter

The same type of spectral analyses are performed for the non zero nodal diameters $n_d = \pm 2$. In this case, the vibration frequency observed in the blade row $R_0$ is shifted because of the Doppler effect. For the nodal diameter $n_d = +2$,

[1] For such small amplitudes of vibration a linear dependence $\overline{F}(f_{\text{ael}}) = \lambda q^*$ of the vibration peak magnitude with respect to the amplitude of vibration $q^*$ is expected. This is confirmed by a careful observation of the plots on Fig. 7b and 8b.

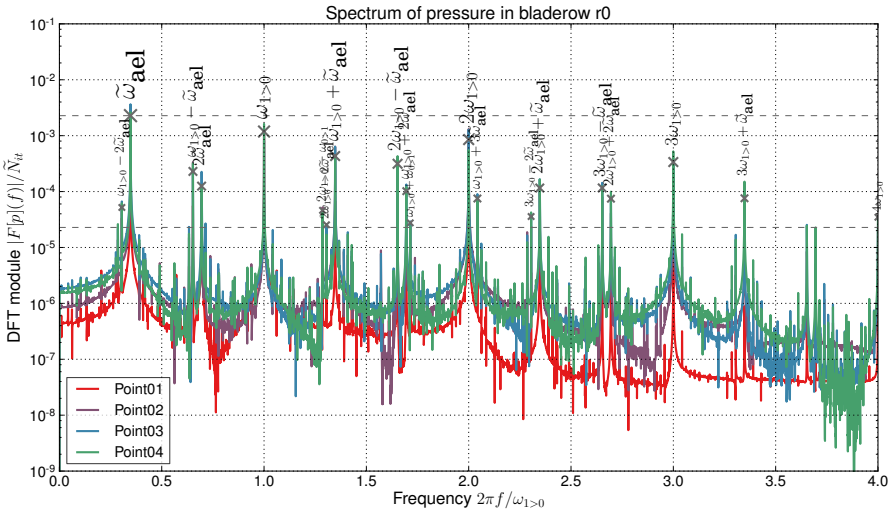


(a) Spectra of probes in $R_0$

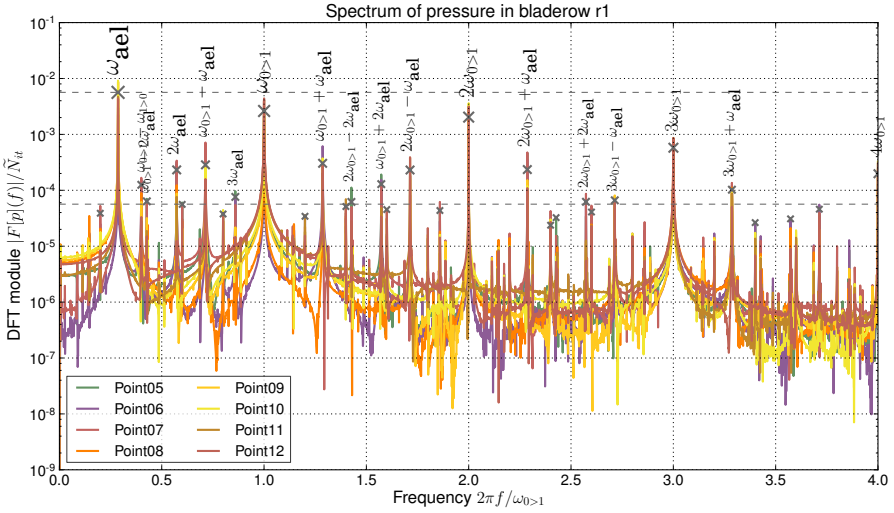


(b) Spectra of probes in $R_1$

**Figure 9**: Comparison of pressure spectra computed with the 2.5D model of the 360° flexible contrafan for the nodal diameter $n_d = +2$ and $q^* = 10^{-3}$.

the shifted frequency is $\widetilde{\omega}_{\text{ael}} = \omega_{\text{ael}} + 2\Delta\Omega = 927$ Hz. The main spinning modes identified from the spectra plotted on figure 9 are again of the same type: the primary spinning modes $(m, 0)$ for $m \in \{1, 2, 3\}$ and $(0, n)$ for $n \in \{1, \ldots, 5\}$ contribute mostly to the unsteady response and secondary spinning modes $(\pm m, \pm n)$ for $m \in \{1, 2, 3\}$ contribute to a lesser extent.

For the nodal diameter $n_d = -2$, the shifted frequency is quite low $\widetilde{\omega}_{\text{ael}} = \omega_{\text{ael}} - 2\Delta\Omega = 164$ Hz. The same type of spinning modes is involved as shown on the spectra plotted on figure 10, but the analyses now reveal in the blade row $R_0$ some clusters of spinning modes centered around the blade passing frequency and its harmonics: since the shifted frequency $\widetilde{\omega}_{\text{ael}}$ is low the secondary spinning modes $(\pm m, n)$ for $m \in \{1, 2\}$ and $n \in \{1, 2, 3\}$ are very close to the primary spinning modes $(0, n)$ for $n \in \{1, 2, 3\}$, hence this effect of clustering. This effect is even more pronounced for $n_d = -3$ since the shifted frequency is $\widetilde{\omega}_{\text{ael}} = 26$ Hz. Such a clustering effect could also appear if the (shifted) vibration frequency (or a harmonic) is close to one of the blade passing frequencies. The simulation of such cases is more challenging since a long time interval has to be computed to capture correctly low frequency perturbations.

The relative magnitude of the 5 main peaks is listed for each nodal diameter in table 4. For non zero nodal diameters, the primary spinning modes are still

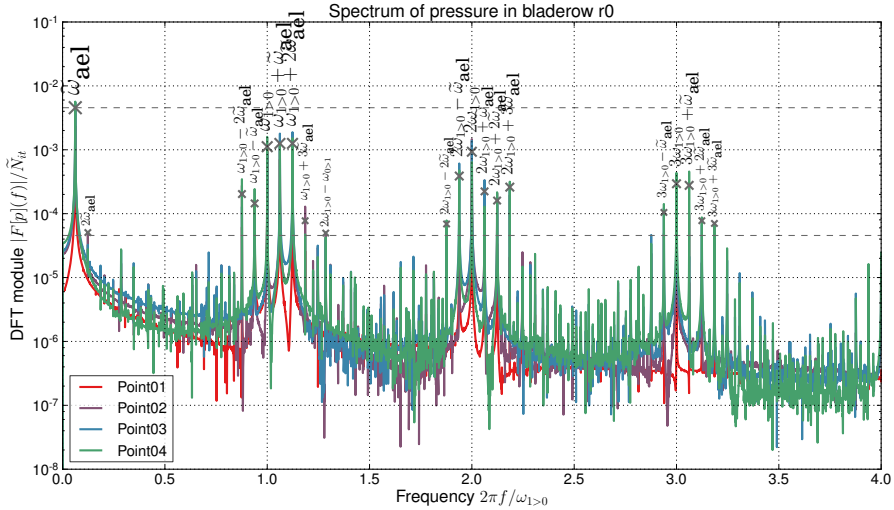


(a) Spectra of probes in $R_0$

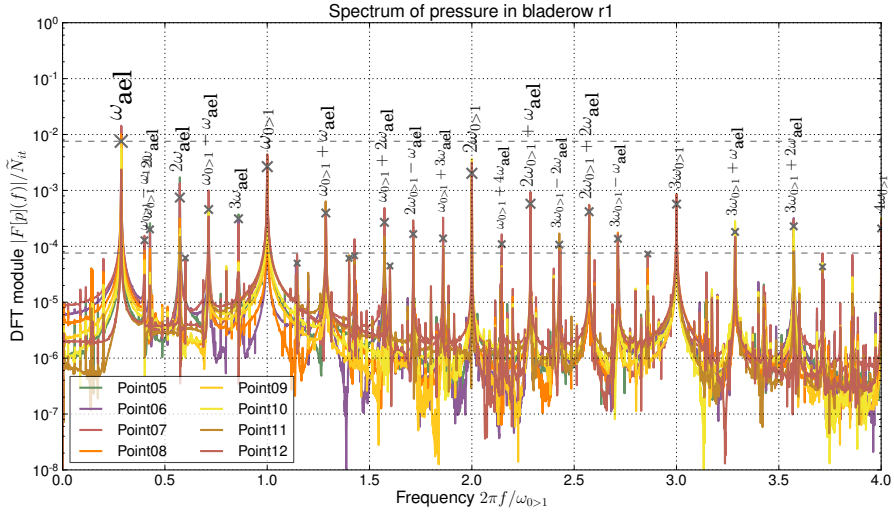


(b) Spectra of probes in $R_1$

**Figure 10**: Comparison of pressure spectra computed with the 2.5D model of the 360° flexible contrafan for the nodal diameter $n_d = -2$ and $q^* = 10^{-3}$.

| | $n_d = 0$ | | $n_d = +2$ | | $n_d = -2$ | |
|---|---|---|---|---|---|---|
| $R_0$ | $\widetilde{\omega}_{\text{ael}}$ | :100% | $\widetilde{\omega}_{\text{ael}}$ | :100% | $\widetilde{\omega}_{\text{ael}}$ | :100% |
| | $\omega_{R_1>R_0} + 2\widetilde{\omega}_{\text{ael}}$ | : 12% | $\omega_{R_1>R_0}$ | : 52% | $\omega_{R_1>R_0} + 2\widetilde{\omega}_{\text{ael}}$ | : 28% |
| | $2\omega_{R_1>R_0}$ | : 11% | $2\omega_{R_1>R_0}$ | : 37% | $\omega_{R_1>R_0} + \widetilde{\omega}_{\text{ael}}$ | : 28% |
| | $\omega_{R_1>R_0}$ | : 10% | $\omega_{R_1>R_0} + \widetilde{\omega}_{\text{ael}}$ | : 19% | $\omega_{R_1>R_0}$ | : 25% |
| | $2\omega_{R_1>R_0} - \widetilde{\omega}_{\text{ael}}$ | : 6% | $3\omega_{R_1>R_0}$ | : 15% | $2\omega_{R_1>R_0}$ | : 20% |
| | $S_d$ | : 1.7 | $S_d$ | : 2.9 | $S_d$ | : 2.5 |
| $R_1$ | $\omega_{\text{ael}}$ | :100% | $\omega_{\text{ael}}$ | :100% | $\omega_{\text{ael}}$ | :100% |
| | $\omega_{R_0>R_1}$ | : 76% | $\omega_{R_0>R_1}$ | : 46% | $\omega_{R_0>R_1}$ | : 35% |
| | $2\omega_{R_0>R_1}$ | : 32% | $2\omega_{R_0>R_1}$ | : 36% | $2\omega_{R_0>R_1}$ | : 27% |
| | $\omega_{R_0>R_1} + \omega_{\text{ael}}$ | : 17% | $3\omega_{R_0>R_1}$ | : 10% | $2\omega_{\text{ael}}$ | : 10% |
| | $3\omega_{R_0>R_1}$ | : 11% | $\omega_{R_0>R_1} + \omega_{\text{ael}}$ | : 5% | $2\omega_{R_0>R_1} + \omega_{\text{ael}}$ | : 8% |
| | $S_d$ | : 2.9 | $S_d$ | : 2.4 | $S_d$ | : 2.4 |

**Table 4**: Relative magnitude of the 5 most significant peaks in the spectral analysis of pressure time histories for different nodal diameters.

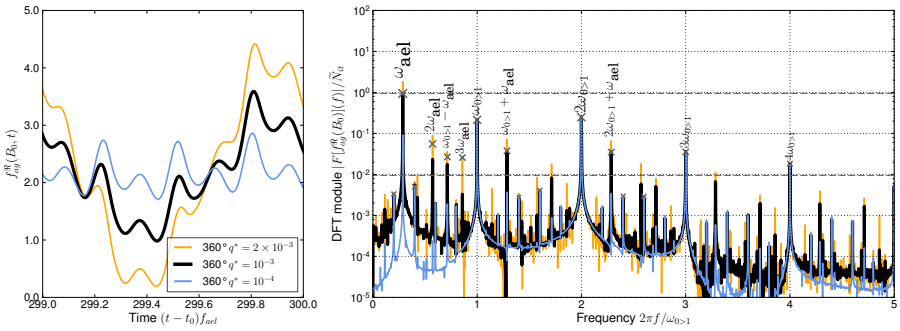


(a) Influence of the amplitude of vibration $q^* \in \{10^{-4}, 10^{-3}, 2\times10^{-3}\}$

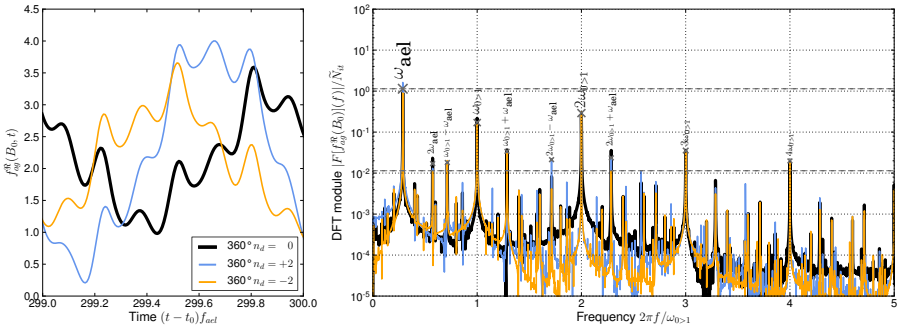


(b) Influence of the pattern of vibration $n_d \in \{0, \pm2\}$

**Figure 11**: Influence of the amplitude and pattern of vibration on the generalized aerodynamic force computed on the reference blade $B_0$.

prominent ($\overline{F}(f_p)/\overline{F}_{\max} \geq 20$ %) and have to be necessarily considered for the approximation of the pressure time series. However the case $n_d = -2$ involves also secondary spinning modes with a significant contribution to the response in the first blade row (up to 28% of the main peak). Such cases will be more challenging for the single passage computations since additional spinning modes have to be included to improve the approximation and to capture accurately the interaction between the unsteady phenomena.

### 4.2.3 Generalized Aerodynamic Forces

One the main purposes of aeroelastic simulations is to evaluate the generalized aerodynamic forces from which the aeroelastic stability can be assessed. This quantity is defined below using the $L^2$ inner product $\langle\cdot,\cdot\rangle_{L^2}$ for complex valued functions as the projection of the aerodynamic force on the structural mode considered to prescribe the motion of the aeroelastic interface:

$$f_{ag}(t) = \langle \boldsymbol{\varphi}(\boldsymbol{x}), \boldsymbol{f}_a(\boldsymbol{x},t)\rangle_{L^2} = \int_{\boldsymbol{x}\in\Gamma} \overline{\boldsymbol{\varphi}}(\boldsymbol{x})\cdot\boldsymbol{f}_a(\boldsymbol{x},t)\,\mathrm{d}s = f_{ag}^{\Re}(t) - \mathrm{i}f_{ag}^{\Im}(t). \quad (28)$$

The last relation is obtained by splitting the complex mode into its real and imaginary parts $\boldsymbol{\varphi} = \boldsymbol{\varphi}^{\Re} + \mathrm{i}\boldsymbol{\varphi}^{\Im}$. The aeroelastic interface which corresponds to the blade surfaces is decomposed as $\Gamma = \bigcup_{k=0}^{N_b-1}\Gamma_k$ and the real (resp. imaginary) part of the generalized aerodynamic force therefore writes using the generic relation with $\mathfrak{C} = \Re$ (resp. $\mathfrak{C} = \Im$):

$$f_{ag}^{\mathfrak{C}}(t) = \sum_{k=0}^{N_b-1} f_{ag}^{\mathfrak{C}}(B_k,t) = \sum_{k=0}^{N_b-1}\int_{\Gamma_k} \boldsymbol{\varphi}^{\mathfrak{C}}(B_k)\cdot\boldsymbol{f}_a(B_k,t)\mathrm{d}s. \quad (29)$$

We focus in the following on the real (resp. imaginary) part of the generalized aerodynamic forces $f_{ag}^{\Re}(B_0,t)$ (resp. $f_{ag}^{\Im}(B_0,t)$) computed on the reference blade since the multichorochronic simulations performed on a single passage only give this contribution to the global generalized aerodynamic force $f_{ag}^{\Re}(t)$ (resp. $f_{ag}^{\Im}(t)$).

| GAF type | $n_d = 0$ | | | $n_d = +2$ | $n_d = -2$ |
|---|---|---|---|---|---|
| | $q^* = 10^{-4}$ | $q^* = 10^{-3}$ | $q^* = 2.10^{-3}$ | $q^* = 10^{-3}$ | $q^* = 10^{-3}$ |
| Local | 2.6 | 1.7 | 1.4 | 1.7 | 1.3 |
| Global | 1.1 | 1.0 | 1.1 | 1.1 | 1.1 |

**Table 5**: Spectral density indicator of the generalized aerodynamic forces for several amplitudes and patterns of vibration.

Figure 11a shows on one hand the influence of the amplitude of vibration on the real part $f_{ag}^{\Re}(B_0, t)$ of the generalized aerodynamic force computed on the reference blade only. The magnitude of the force increases with the amplitude $q^*$ of the excitation since the contribution due to the vibration obviously plays a more important role. Conversely for small amplitudes of vibration ($q^* = 10^{-4}$) the vibration peak magnitude decreases but oscillations in the time history is still significant because of the blade passing phenomenon. The spectral analyses indeed highlight that the magnitude of the peak at $\omega_{\text{ael}}$ evolves almost linearly with $q^*$, but the magnitude of the peaks associated to the blade passage $\omega_{0>1}$ and its harmonics remains constant whatever the amplitude since the phenomenon is decorrelated from the vibration. The peaks associated to the secondary spinning modes involving interactions between the vibration and the blade passage are also directly correlated to the amplitude of vibration and vanish for very small amplitudes. On the other hand, figure 11b shows the influence of the nodal diameter on the generalized aerodynamic force. The magnitude is only slightly changed for the nodal diameters considered, but the spectral content and especially the phase of the time histories are significantly modified. The phase with respect to the harmonic excitation has a direct influence on the stability which therefore strongly depends on the pattern of vibration.

The same type of spinning modes are observed in the spectral analyses of the generalized aerodynamic forces as the one described for pressure time histories. The primary spinning modes corresponding to the vibration, the blade passage and their first harmonics are predominant and should be sufficient to approximate satisfactorily the generalized aerodynamic forces with multichorochronic computations. Secondary spinning modes should however be added for a more accurate approximation when their magnitudes are of the same order as those of the primary spinning modes.

Table 5 indicates the values of the spectral density indicator for the global and local generalized aerodynamic forces. This quantity decreases when the amplitude of vibration increases since the time history becomes mainly governed by the vibration. For smaller amplitudes (*e. g.* for $q^* \approx 10^{-4}$ and $n_d = 0$) the spectral density indicator is larger because both unsteady phenomena contribute almost equally to the response. In the limit of extremely small amplitudes, the response would be essentially governed by the blade passing frequency and its harmonics and the spectral density indicator would thus converge to the value obtained for the perfectly rigid case. The spectral densities are a bit smaller than those computed from the pressure probes since the generalized aerodynamic force is an integrated quantity which filters out locally complicated nonlinear phenomena inducing a high spectral density. It can also be observed from table 5 that the spectral density indicator of the global generalized aerodynamic force is always close to 1, which means that the time response is almost periodic. This filtering effect comes from the summation of all the contributions $f_{ag}^{\mathfrak{C}}(B_k, t)$: the spinning modes with wave numbers different from the nodal diameter of the structural mode considered cancel out and the spinning mode associated to the vibration frequency is consequently the only one remaining after the projection on all blades.

This filtering effect is illustrated on figure 12 which shows the global and local generalized aerodynamic forces plotted against the dimensionless amplitude of vibration. When the response is linear (and thus periodic like the global

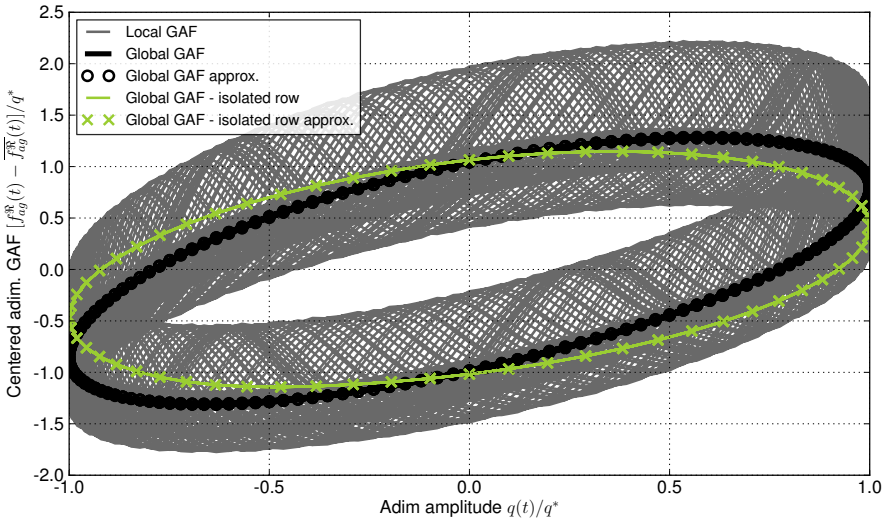


**Figure 12**: Comparison of the local and global generalized aerodynamic forces computed on the reference blade or all blades for $q^* = 10^{-3}$ and $n_d = 0$.

generalized aerodynamic force in the present case) with respect to the harmonic excitation, the Lissajous figures are elliptic. The local generalized aerodynamic force exhibits on the contrary a nonlinear response with a much more complicated limit cycle characterized by a kind of thick ellipse for an infinite time interval. The Lissajous curve is also plotted on figure 12 for the isolated vibrating blade row $R_1$. The response is in this case obviously periodic since the only source of unsteadiness comes from the vibration. The magnitude, but above all the phase of the limit cycle has changed, which means that the aeroelastic stability is different if the effect of the blade passage is taken into account or not. The global generalized aerodynamic forces for the isolated and stage configurations have been approximated by a sinusoid of the type $A_0 + A\sin(\omega_{ael}t + \psi)$. The blade passing effect induces an increase of about 14% of the amplitude $A$ and a change of the phase $\psi$ of about 18%. Such differences can be amplified depending on the nodal diameter considered, especially when the nodal diameter of excitation coincides with the number of blades $N_{b,0}$ in the adjacent blade row.

### 4.3 Single Passage Computations with Multichorochronic Boundary Conditions

Computations are now performed on a single passage using multichorochronic boundary conditions for which several spinning modes have to be given a priori to approximate the flow field. The spectral analyses performed previously on the full annulus configuration have confirmed that few spinning modes are predominant and should provide an accurate approximation. The influence of different parameters related to the multichorochronic approximation is first investigated. Then single passage and full annulus computations are compared for different nodal diameters and finally the influence of the relaxation parameter on the convergence is illustrated on 3D computations.

#### 4.3.1 Influence of the Number of Harmonics for $n_d = 0$

The influence of the number of harmonics $N_{h,p}$ considered for each spinning mode (see Eq. (18)) is investigated here for the nodal diameter $n_d = 0$. Only the primary spinning modes $(1, 0)$ and $(0, 1)$ corresponding to the vibration and the blade passage are considered; the set of spinning modes is therefore $\mathcal{SP} = \mathcal{SP}_1$ with $N_{\text{sp}} = 2$.

The time histories and spectral analyses of probes 03 and 05 in $R_0$ and $R_1$ respectively are presented on figures 13a and 13b. A zoom on a single vibration

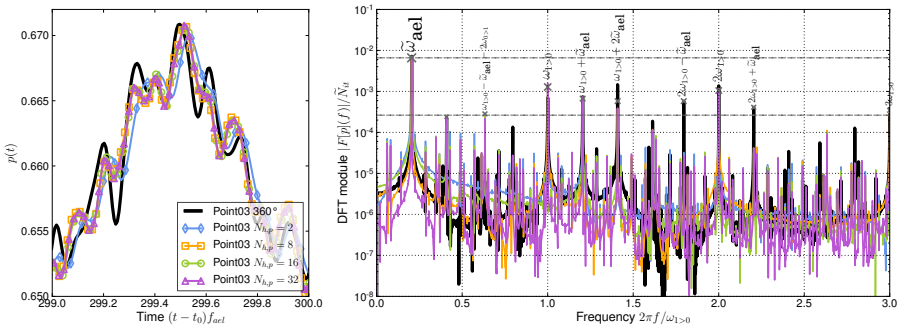


(a) Time history and spectra of probe 03 in $R_0$

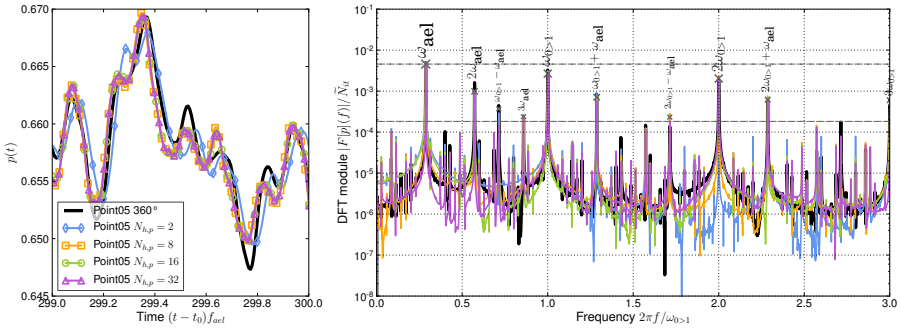


(b) Time history and spectra of probe 05 in $R_1$

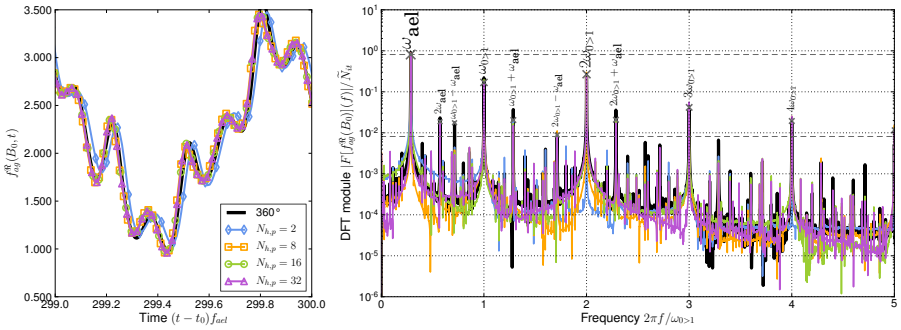


(c) Time history and spectra of the local generalized aerodynamic force

**Figure 13**: Influence of the number of harmonics $N_{h,p}$ on the multichorochronic approximation using $N_{\text{sp}} = 2$ primary spinning modes ($n_d = 0$, $q^* = 10^{-3}$).

period is plotted to appreciate the small discrepancies on the time histories. For each probe the agreement with respect to the full annulus simulation is satisfactory for the time histories which are qualitatively well reproduced using the multichorochronic approximation even with a number of harmonics as small as $N_{h,p} = 2$. There is only little improvement when increasing the number of harmonics beyond $N_{h,p} = 8$; low harmonics only indeed contribute significantly to the response as expected from the spectral analyses of section 4.2. The accuracy of the multichorochronic approximation is evaluated by means of the following averaged relative error formulated for continuous functions in the $L^2([t_0; t_0 + T])$ Hilbert space embedded with the norm $||g||^2_{\widetilde{L}^2} = \int_\tau^{\tau+T_{\text{ael}}} g^2(\tau)\mathrm{d}\tau$ for $\widetilde{L}^2 = L^2([\tau; \tau + T_{\text{ael}}])$ defined on a time window covering a vibration period

$$\epsilon = \frac{1}{N_{\text{probes}}} \sum_{k=1}^{N_{\text{probes}}} \epsilon_{P_k} \text{ with } \epsilon_{P_k} = \int_{t_0}^{t_0+T} \frac{\|s(P_k,\tau) - \widehat{s}(P_k,\tau)\|^2_{\widetilde{L}^2}}{\|s(P_k,\tau) - \overline{s}(P_k)\|^2_{\widetilde{L}^2}} \mathrm{d}\tau \qquad (30)$$

where $s(P_k, t)$ is an aerodynamic quantity (like the pressure) recorded by the probe $P_k$, $\widehat{s}(P_k, t)$ is its multichorochronic approximation and $\overline{s}(P_k)$ is the time average of $s(P_k, t)$; the previously defined error is typically time-averaged on an interval $T = 50T_{\text{ael}}$ covering a sufficiently large number of vibration cycles. The error and the standard deviation $\sigma = \sum_k (\epsilon_{P_k} - \epsilon)^2 / N_{\text{probes}}$ are listed in table

**Table 6**: Averaged relative error computed from the time histories using an increasing number of harmonics $N_{h,p}$.

| $N_{h,p}$ | $N_{\text{sp}}$ | $n_d$ | $\epsilon \pm \sigma$ | $\epsilon_{\text{GAF}}$ |
|---|---|---|---|---|
| 2 | 2 | 0 | 18.4 %±9.7 % | 10.0 % |
| 8 | 2 | 0 | 9.6 %±4.4 % | 2.8 % |
| 16 | 2 | 0 | 6.4 %±3.3 % | 1.4 % |
| 32 | 2 | 0 | 7.5 %±2.8 % | 1.9 % |

6 for several number of harmonics $N_{h,p}$ used in the approximation. The errors are reduced when the number of harmonics increases from $N_{h,p} = 2$ to 16, but it can be observed that increasing too much this parameters leads to a slight increase of the error when $N_{h,p} = 32$.

The spectral analyses presented on figures 13a and 13b show qualitatively a good agreement with respect to the full annulus computation. Apart from the predominent peaks, the magnitudes of the other peaks are however often over- or under-estimated. For such a simulation based only on the primary spinning modes, one should expect a satisfactory accuracy on the magnitudes of the peaks corresponding to these modes only. This is the case here since the magnitudes for $\omega_{\text{ael}}$, $\omega_{0>1}$, $\omega_{1>0}$ and their first harmonics are quite well captured. The magnitudes of the secondary spinning modes are less well predicted since these modes develop inside the fluid domain where the probes are located but they are not propagated through the domain boundaries since they are not prescribed in the multichorochronic approximation.

The multichorochronic computations tend to amplify the magnitude of certain spinning modes corresponding to complicated interactions (*e. g.* the peak at $\omega_{1>0} - \widetilde{\omega}_{\text{ael}} - 2\omega_{0>1}$ in $R_0$, see Fig. 13a) which are minor or even absent from the spectral analysis of the full annulus computation. Such an amplification was already observed with the single frequency chorochronic simulation of the rigid stage (see Fig. 5a) where a series of peaks corresponding to $\Delta\Omega$ and its harmonics was amplified compared to the full annulus computation. This phenomenon is a limitation of the multichorochronic approach since the robustness of the simulation can be jeopardized if such artificial components are not contained. For the present multichorochronic computation the phenomenon appears only for $N_{h,p} > 2$ and a good practice for such simulations is to consider only a relatively small number of harmonics, or to use a smaller relaxation parameter $\eta_{p,k}$ for higher harmonics $k \gg 1$. Besides it has been observed that if close frequencies are included in the multichorochronic approximation the convergence of the Fourier coefficients is poor. If two frequencies $k_i\omega_p$ and $k_j\omega_q$ are very close, one of them is removed (preferably the highest harmonic $k_i$ if $k_i > k_j$).

The last plots on figure 13c present the time histories and spectra of the local generalized aerodynamic force. The agreement is also very good even with few harmonics. The values of the relative error computed with an expression similar to Eq. (30) with $s(t) = f_{ag}^{\Re}(B_0, t)$ are given in table 6. The error decreases significantly when the number of harmonics increases until $N_{h,p} = 16$ and then increases slightly for $N_{h,p} = 32$.

### 4.3.2 Influence of the Number of Spinning Modes

Additional modes corresponding to the main peaks identified from full annulus computations are now included to improve the multichorochronic approximation. A first simulation with $N_{\text{sp}} = 2$ is based on the set of primary spinning modes $\mathcal{SP}_1 = \{(1,0),(0,1)\}$. In view of the full annulus computations (see table 3), a second simulation is performed with a multichorochronic approximation using $N_{\text{sp}} = 4$ spinning modes in each blade row comprising the set $\mathcal{SP}_1$ and such that $\mathcal{SP}_2 = \{(1,1),(2,1)\}$ in $R_0$ and $\mathcal{SP}_2 = \{(1,1),(1,2)\}$ in $R_1$. A third simulation using $N_{\text{sp}} = 8$ spinning modes comprising the set $\mathcal{SP}_1$ and such that $\mathcal{SP}_2 = \{(1,1),(-1,1),(2,1),(-2,1),(1,2),(-1,2)\}$ in $R_0$ and $R_1$ is finally considered. The number of harmonics for secondary spinning modes is always set

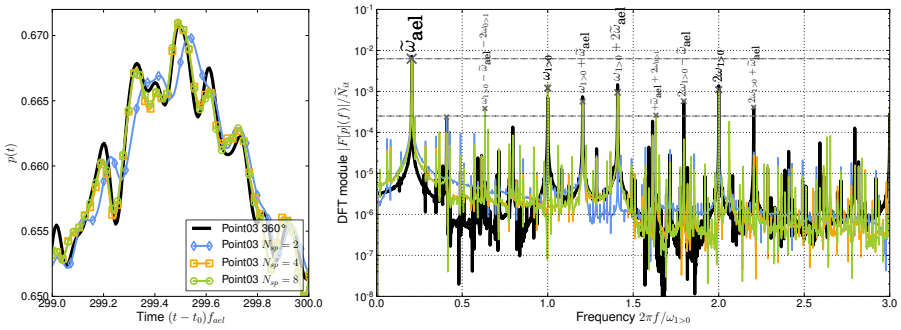


(a) Time history and spectra of probe 03 in $R_0$

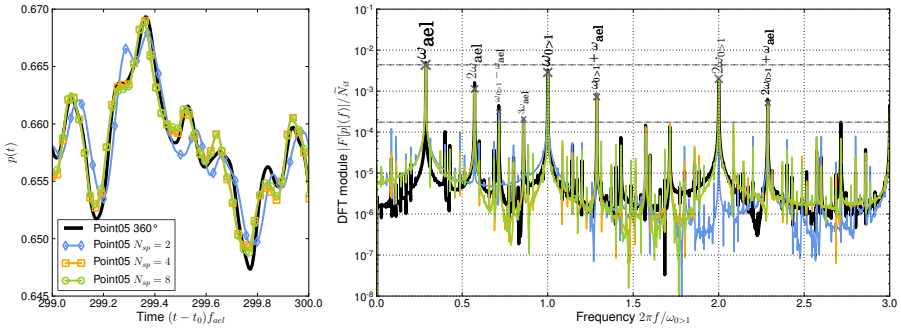


(b) Time history and spectra of probe 05 in $R_1$

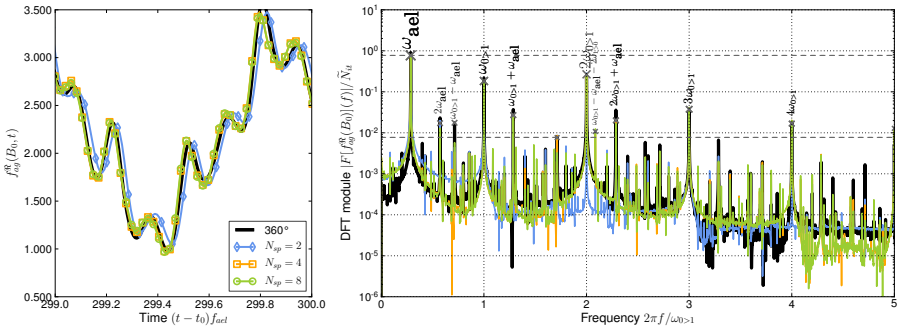


(c) Time history and spectra of the local generalized aerodynamic force

**Figure 14**: Influence of the number of spinning modes $N_{\text{sp}}$ on the multichorochronic approximation ($n_d = 0$, $q^* = 10^{-3}$).

to $N_{h,p} = 1$.

A single period of the time histories and the spectral analyses are plotted on figure 14a and 14b for two probes. The time response is improved with $N_{\text{sp}} = 4$ instead of $N_{\text{sp}} = 2$ spinning modes, but as expected in view of the spectral analyses summarized in table 3, there is only little change when increasing the number of spinning modes from $N_{\text{sp}} = 4$ to 8 since the magnitudes of the secondary peaks are much smaller. The values of the errors listed in table 7 quantify this slight improvement compared to the approximation with $N_{\text{sp}} = 2$ and $N_{h,p} = 8$. The agreement is also excellent for the local generalized aerodynamic force which is plotted on figure 14c, even with only $N_{\text{sp}} = 2$ spinning modes. Here again the complicated linear frequency combination $\omega_{1>0} - \widetilde{\omega}_{\text{ael}} - 2\omega_{0>1}$ is amplified as the number of spinning modes is increased. As a conclusion, a small number of spinning modes $N_{\text{sp}} = 2$ and harmonics $N_{h,p} \leq 8$ is preferably used to avoid the introduction of artificial spectral content.

The accuracy of the multichorochronic approximation is finally investigated for $n_d = \pm 2$. The time histories and spectra are plotted on figures 15 and 16 for the probe 03 located in $R_0$ and the generalized aerodynamic force. The frequency shift caused by the Doppler effect is well captured in the time history of probe 03 for both nodal diameters. Once again the accuracy of the approx-

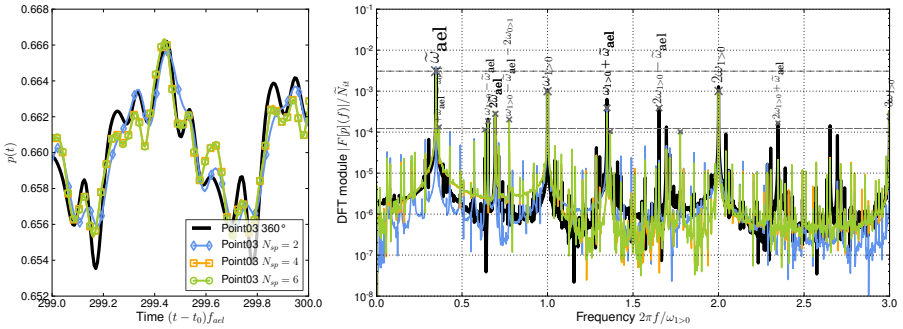


(a) Time history and spectra of probe 03 in $R_0$

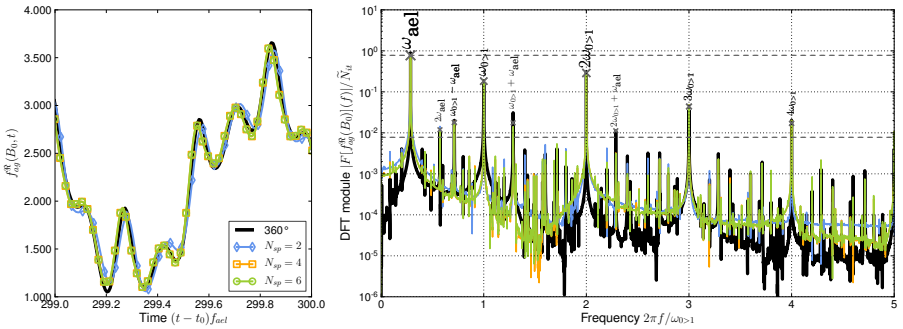


(b) Time history and spectra of the local generalized aerodynamic force

**Figure 15**: Influence of the number of spinning modes $N_{\text{sp}}$ on the multichorochronic approximation ($n_d = +2$, $q^* = 10^{-3}$).

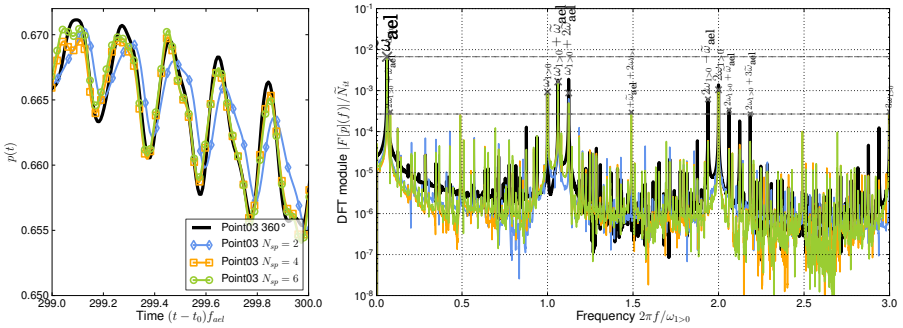


(a) Time history and spectra of probe 03 in $R_0$

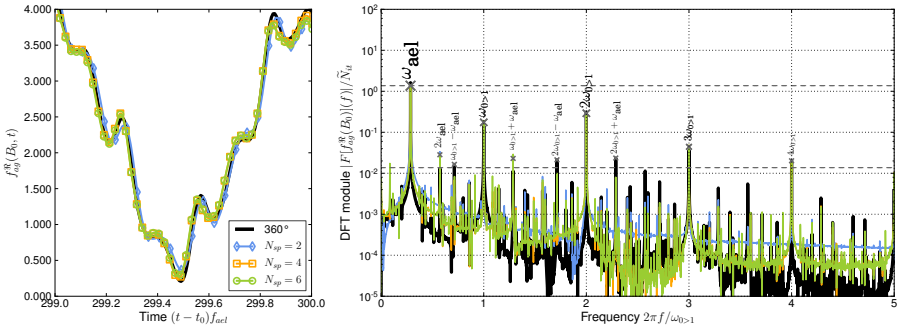


(b) Time history and spectra of the local generalized aerodynamic force

**Figure 16**: Influence of the number of spinning modes $N_{\text{sp}}$ on the multichorochronic approximation ($n_d = -2$, $q^* = 10^{-3}$).

| $N_{h,p}$ | $N_{\text{sp}}$ | $n_d$ | $\epsilon \pm \sigma$ | $\epsilon_{\text{GAF}}$ |
|---|---|---|---|---|
| 8 | 2 | 0 | 9.6 %±4.4 % | 2.8 % |
| 8 | 4 | 0 | 5.0 %±2.3 % | 1.7 % |
| 8 | 8 | 0 | 5.0 %±2.5 % | 1.7 % |
| 4 | 2 | +2 | 20.1 %$\pm^{17.7}_{\%}$ | 1.0 % |
| 4 | 4 | +2 | 12.6 %$\pm^{10.0}_{\%}$ | 0.7 % |
| 4 | 6 | +2 | 12.6 %$\pm^{9.7}_{\%}$ | 0.7 % |
| 4 | 2 | −2 | 17.6 %$\pm^{17.0}_{\%}$ | 2.3 % |
| 4 | 4 | −2 | 12.2 %± 9.8% | 1.4 % |
| 4 | 6 | −2 | 12.3 %± 9.9% | 1.4 % |

**Table 7**: Averaged relative error computed from the time histories using an increasing number of spinning modes $N_{\text{sp}}$.

imation is improved when the number of spinning modes is increased and the agreement is satisfactory for the time histories of pressure and even excellent for the generalized aerodynamic force. However the magnitudes of some secondary spinning modes are difficult to capture, even if the corresponding modes are explicitly prescribed in the multichorochronic approximation. Some complicated frequency interactions are here again over-estimated compared with full annulus computations when the number of spinning modes becomes large. These discrepancies are nevertheless minor for aeroelastic purposes since the error on the generalized aerodynamic force prediction with the multichorochronic approximation is less than 3% for the different nodal diameter considered (see table 7).

#### 4.3.3 Influence of the Relaxation Parameter for 3D Computations

Simulations with the 3D model are very time consuming since they are parameterized so as to obtain a sufficiently long converged time history from which an accurate spectral analysis with a frequency resolution $\delta f = (\widetilde{N}_{\text{it}}\delta t)^{-1} \lessapprox \mathcal{O}(10)$ Hz can be performed. The total number of iterations $N_{\text{it}} = N_{\text{trans}} + \widetilde{N}_{\text{it}}$ comprises $N_{\text{trans}}$ iterations corresponding to the transient after which a converged quasi-periodic state covering $\widetilde{N}_{\text{it}}$ iterations is reached and can be used for the spectral analysis. However the speed of convergence is characterized by the length of the transient $N_{\text{trans}}$ which directly depends on the relaxation parameter $\eta$. Assuming that the convergence depends linearly on the relaxation parameter, if $N_{\text{trans}}$ is the number of iterations for the transient in an ideal case ($\eta = 1.0$), then the length of the transient increases as $N_{\text{trans}}/\eta$ when $0 < \eta \leq 1$. Increasing the relaxation parameter is therefore a clever way to shorten the transient but a compromise has to be found since too large values may hinder the convergence.

An illustration of the generalized aerodynamic force transients is given on the left of figure 17 for $\eta = 0.1$, 0.5 and 0.9. The convergence to a quasi-periodic state is reached much more quickly with $\eta = 0.9$ than with $\eta = 0.1$. The convergence of local quantities like the pressure on a given probe can be a bit longer than the one given roughly here for the generalized aerodynamic force. Once the convergence is reached, the time history is the same whatever the value of $\eta$. This is confirmed by the spectra plotted on the right showing a good agreement whatever the value of the relaxation parameter $\eta$. In the present case the simulation is stable even with $\eta = 0.9$ since the primary spinning modes only are considered. Lower values of the relaxation parameters should be used if more spinning modes are considered, at least for the secondary modes. In this case the transient would inevitably increase but one can expect a better

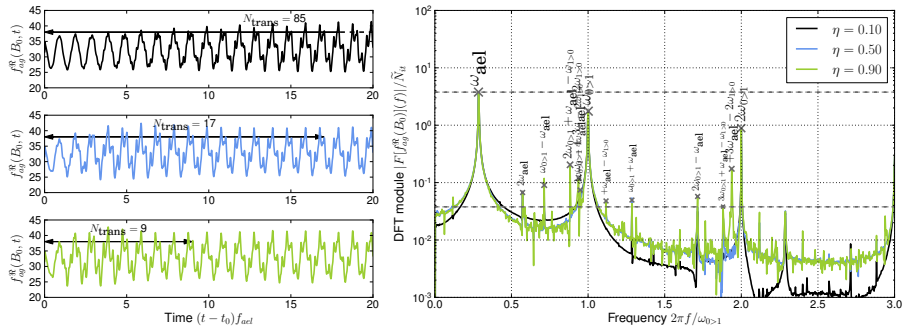


**Figure 17**: Comparison of generalized aerodynamic force transients and spectra for different values of the relaxation parameter $\eta$.

accuracy of the solution.

Such a simulation of the 3D model performed with only 8 processors requires a CPU time of about 22 days if the relaxation parameter is set to $\eta = 0.1$ and the target frequency resolution is $\delta f \sim 5$ Hz. Half of the CPU time is however spent to converge the solution. Increasing the relaxation parameter to $\eta = 0.9$ for example shortens the transient and spectral analyses can be performed with the same frequency resolution from a computation which only requires a CPU time of about 12 days.

The transient would be even shorter with a full annulus computation since the flow is not approximated on the boundaries and there is no need to converge some Fourier coefficients. However the full annulus computation would monopolize about 100 processors of a cluster if an equivalent parallelization of the 3D model was considered. The single passage computation with multichorochronic boundary conditions provides thus a good compromise between the accuracy of the solution and the resources required (number of processors, memory and CPU time).

## 5 Conclusion

In this paper a multichorochronic approximation of the flow field on the boundaries of a single passage turbomachinery stage has been investigated in the time domain using RANS equations. A detailed analysis of the spectral content of such aeroelastic computations with stage effects has been performed to identify the main spinning modes contributing to the response. Accurate solutions have then been obtained using a much smaller single passage model instead of the large full annulus model. It has been shown that even with a small number of spinning modes and harmonics, the generalized aerodynamic forces are outstandingly well reproduced for the different nodal diameters considered in this paper. Further work will need to investigate the potential of this approach for other operating points and configurations and also to derive an expression of the global generalized aerodynamic forces from the local expression provided by such single passage simulations so that the aeroelastic stability of the whole blade row could be assessed while taking into account the stage effects using a single passage model.

## Acknowledgments

This work was supported by the Direction Générale de l'Aviation Civile (DGAC) under the Convention n° 2009 93 0834 for the research project Aerovista. Thanks to Snecma for providing the contrafan model VITAL.

## References

[1] A. Arnone and R. Pacciani. Rotor-stator interaction analysis using the Navier-Stokes equations and a multigrid method. *J. Turbomach.*, 118(4):

679–89, 1996. URL dx.doi.org/10.1115/1.2840923.

[2] D.H. Buffum. Blade row interaction effects on flutter and forced response. In *29th AIAA/SAE/ASME/ASEE Joint Propuls. Conf.*, number 2084, Monterey, 1993. URL dx.doi.org/10.2514/6.1993-2084.

[3] L. Cambier, S. Heib, and S. Plot. The Onera elsA CFD software: input from research and feedback from industry. *Mechanics & Industry*, 14(3): 159–74, 2013. URL dx.doi.org/10.1051/meca/2013056.

[4] L. Castillon. Evaluation of a multiple frequency phase-lagged method for unsteady numerical simulations of multistage turbomachinery. In *28th Int. Counc. Aeronaut. Sci.*, Brisbane, 2012. URL www.icas.org/ICAS_ARCHIVE/ICAS2012/PAPERS/056.PDF.

[5] K. Ekici and K.C. Hall. Nonlinear analysis of unsteady flows in multistage turbomachines using harmonic balance. *AIAA J.*, 45(5):1047–57, 2007. URL dx.doi.org/10.2514/1.22888.

[6] J. I. Erdos, E. Alzner, and W. McNally. Numerical solution of periodic transonic flow through a fan stage. *AIAA J.*, 15(11):1559–68, 1977. URL dx.doi.org/10.2514/3.60823.

[7] D. J. Ewins. Vibration characteristics of bladed disc assemblies. *J. Mech. Eng. Sci.*, 15:165–86, 1973. URL dx.doi.org/10.1243/JMES_JOUR_1973_015_032_02.

[8] A. Fourmaux. Assessment of a low storage technique for multi-stage turbomachinery Navier-Stokes computations. In *ASME Winter Annu. Meet.*, Chicago, 1994.

[9] G. A. Gerolymos, G. J. Michon, and J. Neubauer. Analysis and application of chorochronic periodicity in turbomachinery rotor/stator interaction computations. *AIAA J.*, 18(6):1139–52, 2002. URL dx.doi.org/10.2514/2.6065.

[10] G.A. Gerolymos and V. Chapin. Expression généralisée de la périodicité chrorochronique dans l'interaction entre aubages de turbomachines. *Rech. Aérosp.*, 5:69–73, 1991.

[11] M.B. Giles. Calculation of unsteady wake/rotor interaction. *J. Propuls. Power*, 4(4):356–62, 1988. URL dx.doi.org/10.2514/3.23074.

[12] K.C. Hall and K. Ekici. Multistage coupling for unsteady flows in turbomachinery. *AIAA J.*, 43(3):624–32, 2005. URL dx.doi.org/10.2514/1.8520.

[13] L. He. Method of simulating unsteady turbomachinery flows with multiple perturbations. *AIAA J.*, 30(11):2730–35, 1992. URL dx.doi.org/10.2514/3.11291.

[14] L. He. Fourier methods for turbomachinery applications. *Prog. Aerosp. Sci.*, 46:329–41, 2010. URL dx.doi.org/10.1016/j.paerosci.2010.04.001.

[15] L. He, T. Chen, R. G. Wells, Y. S. Li, and W. Ning. Analysis of rotor-rotor and stator-stator interferences in multi-stage turbomachines. *J. Turbomach.*, 124(4):564–71, 2002. URL dx.doi.org/10.1115/1.1508382.

[16] X.Q. Huang, L. He, and D.L. Bell. Influence of upstream stator on rotor flutter stability in a low pressure steam turbine stage. *J. Power Energy*, 220(1):25–35, 2006. URL dx.doi.org/10.1243/095765005X69170.

[17] N.H. Kemp and W.R. Sears. Aerodynamic interference between moving blade-rows. *J. Aeronaut. Sci.*, 20(9):585–97, 1953. URL dx.doi.org/10.2514/8.2758.

[18] F. Lane. System mode shapes in the flutter of compressor blade rows. *Journal of the Aeronautical Sciences*, 23(1):54–66, 1956. URL dx.doi.org/10.2514/8.3502.

[19] H.D. Li and L. He. Blade aerodynamic damping variation with rotor-stator gap: a computational study using single-passage approach. *J. Turbomach.*, 127(3):573–79, 2005. URL dx.doi.org/10.1115/1.1928932.

[20] C. Mari and R. Parker. Collaborative european aero-engine environmental research projects led by Snecma and Rolls-Royce. In *24th Int. Counc. Aeronaut. Sci.*, Yokohama, 2004. URL www.icas.org/ICAS_ARCHIVE/ICAS2004/PAPERS/561.PDF.

[21] J. Neubauer. *Aérodynamique 3-D instationnaire des turbomachines axiales multi-étages*. PhD thesis, University of Paris 6, 2004. URL julien.neubauer.free.fr/THESE_JN.pdf.

[22] M. T. Rahmati, L. He, D. X. Wang, Y. S. Li, R. G. Wells, and S. K. Krishnababu. Nonlinear time and frequency domain methods for multirow aeromechanical analysis. *Journal of Turbomachinery*, 136(4):041010–1–10, 2014. URL dx.doi.org/10.1115/1.4024899.

[23] F. Sicot, T. Guédeney, and G. Dufour. Time-domain harmonic balance method for aerodynamic and aeroelastic simulations of turbomachinery flows. *International Journal of Computational Fluid Dynamics*, 27(2):68–78, 2012. URL dx.doi.org/10.1080/10618562.2012.740021.

[24] P. D. Silkowski and K. C. Hall. A coupled mode analysis of unsteady multistage flows in turbomachinery. *J. Turbomach.*, 120(3):410–22, 1998. URL dx.doi.org/10.1115/1.2841732.

[25] S.N. Smith. Discrete frequency sound generation in axial flow turbomachines. Reports and Memoranda No 3709, Aeronaut. Res. Counc., 1972. URL citeseerx.ist.psu.edu/viewdoc/download?doi=10.1.1.226.6174&rep=rep1&type=pdf.

[26] P.R. Spalart and S.R. Allmaras. A one equation turbulence model for aerodynamic flows. In *30th Aerosp. Sci. Meet. Exhib.*, number 0439 in AIAA, Reno, 1992. URL dx.doi.org/10.2514/6.1992-439.

[27] S. C. Stapelfeldt and L. di Mare. A method for modelling flow past non-axisymmetric configurations on reduced passage counts. In *13th Int. Symp. Unsteady Aerodyn. Aeroacoust. Aeroelast. Turbomach.*, number ISUAAAT13-S9-1, Tokyo, 2012.

[28] D.-M. Tran, C. Liauzun, and C. Labaste. Methods of fluid-structure coupling in frequency and time domains using linearized aerodynamics for turbomachinery. *J. Fluids Struct.*, 17(8):1161–80, 2003. URL dx.doi.org/10.1016/S0889-9746(03)00068-9.

[29] J.M. Tyler and T.G. Soffrin. Axial flow compressor noise studies. *SAE Trans.*, 70:309–32, 1962. URL dx.doi.org/10.4271/620532.

[30] R. Valid and R. Ohayon. Théorie et calcul statique et dynamique des structures à symétries cycliques. *Rech. Aérosp.*, 4:251–63, 1985. Presented at the XVI$^{th}$ Int. Congr. Theor. Appl. Mech. (IUTAM), 1984, under the title of *Static and dynamic analysis of cyclically symmetric structures*.